# IMPACT OF IONIZING RADIATION AND ELECTRON INJECTION ON CARRIER TRANSPORT PROPERTIES IN NARROW AND WIDE BANDGAP SEMICONDUCTORS

by

JONATHAN DAVID LEE
M.S. University of Central Florida, 2015
B.S. University of Central Florida, 2012

A dissertation submitted in partial fulfillment of the requirements
for the degree of Doctor of Philosophy
in the Department of Physics
in the College of Sciences
at the University of Central Florida
Orlando, Florida

Summer Term
2018

Major Professors: Elena Flitsiyan & Leonid Chernyak

© 2018 Jonathan Lee

## ABSTRACT

This study investigated the minority carrier properties of wide and narrow bandgap semiconductors. Included specifically are wide bandgap materials GaN and $\beta$-$Ga_2O_3$, and narrow bandgap InAs/GaSb type-II strain-layer superlattice. The importance of minority carrier behavior in bipolar device performance is utmost because it is the limiting component in current conduction. The techniques used to determine minority carrier properties include electron beam induced current (EBIC) and cathodoluminescence (CL) spectroscopy. The CL spectroscopy is complemented with time-resolved CL (TRCL) for direct measurement of carrier radiative recombination lifetime.

The minority carrier properties and effect of high energy radiation is explored. The GaN TRCL results suggested an activation energy effecting carrier lifetime of about 90 meV which is related to nitrogen vacancies. The effects of $^{60}Co$ gamma radiation are demonstrated and related to the effects of electron injection in GaN-based devices. The effects of various high energy radiations upon Si-doped $\beta$-$Ga_2O_3$ minority carrier diffusion length and radiative lifetime are measured. The non-irradiated sample thermal activation energies found for minority carrier diffusion length were 40.9 meV, related to shallow Si-donors in the material. The CL results demonstrate that the bandgap of 4.9 eV is slightly indirect. The thermal activation energy decreased on 1.5 MeV electron irradiation but increased for 10 MeV proton irradiation. The increase in energy was related to higher order defects and their complexes, and influenced recombination lifetime significantly. Finally, the diffusion length is reported for narrow bandgap InAs/GaSb superlattice structure and the effect of $^{60}Co$ gamma radiation is demonstrated.

In general, the defects introduced by high energy radiations decreased minority carrier diffusion length, except for $^{60}Co$ gamma on AlGaN/GaN HEMT devices and high-temperature proton irradiated β-$Ga_2O_3$.

## ACKNOWLEDGMENT

I would like to express my gratitude for the support of Elena Flitsiyan, whose insight and guidance proved invaluable to my academic success and professional development.

For the inspiration of our scientific forefathers, Sir Isaac Newton, Georg Ohm, Michael Faraday, James Clerk Maxwell, Max Planck, Никола Тесла, and Лев Ландáу. For the lives of Galileo Galilei, Ludwig Boltzmann, and Józef Wroński. For the correct, yet inexplainable, judgement of Robert Milikan, and for the often-unrecognized ingenuity of his student Harvey Fletcher. With extreme determination and ambition, these adventurers sook out challenges which ultimately consumed some, but paved the way for the advancement of mathematics, technology, culture, and quality of life for the rest of sustained human civilization. In some cases, their foresight was so strong, that even their peers could not see their brilliance until they had long shuffled off their mortal coil. Their sacrifices are memorialized in the name of physical units, constants, equations, and laws. Their words linger, to guide us as we learn, and to tantalize us as we continue to wonder what secrets remain. I acknowledge their intrepid nature and submit my gratitude.

*For Alena, and for my family. Because their support continues to allow me to grow and thrive.*

# TABLE OF CONTENTS

LIST OF FIGURES ..... ix
LIST OF TABLES ..... x
LIST OF ABBREVIATIONS ..... xi
PHYSICAL CONSTANTS ..... xiii
CHAPTER I – INTRODUCTION ..... 1
1.1 Background ..... 1
1.1.1 Types of Recombination & Luminescence ..... 4
1.1.2 Types of High Energy Radiation ..... 4
1.2 Structural overview of GaN, β-$Ga_2O_3$ and InAs/GaSb (T2SLS) ..... 6
1.2.1 Gallium Nitride ..... 6
1.2.2 Gallium Sesquioxide ..... 7
1.2.3 InAs/GaSb Type II Strain-Layer Superlattice ..... 8
1.3 Trap States in GaN, β-$Ga_2O_3$, and InAs/GaSb T2SLS ..... 9
1.3.1 Activation Energy, $E_a$ ..... 9
1.4 Cathodoluminescence Spectroscopy ..... 9
1.4.1 Decay Lifetime, τ ..... 10
1.5 Minority Carrier Diffusion Length Effect on Device Performance ..... 11
1.6 Dissertation Outline ..... 12
CHAPTER II – EXPERIMENTAL SETUP & TECHNIQUE ..... 14
2.1 Sample Characterization ..... 14
2.1.1 Semiconductor Junctions ..... 14
2.2 Sample Irradiation ..... 16
2.3 Generation Volume & Electron Range ..... 18
2.4 Electron Beam-Induced Current (EBIC) ..... 19
2.4.1 EBIC Setup ..... 20
2.4.2 Determination of L ..... 22
2.4.3 Validity of the Method ..... 23
2.4.4 Thermal Activation Energy of Diffusion ..... 23
2.5 Cathodoluminescence Technique ..... 24
2.5.1 CL Setup ..... 24
2.5.2 Limitations of the Technique ..... 27

2.5.3 Thermal Activation Energy of Luminescence ........ 28
CHAPTER III – RESULTS & DISCUSSION ........ 30
3.1 Minority Carrier Transport Properties in Gallium Nitride ........ 30
3.1.1 Prior State of the Art ........ 30
3.1.2 Cathodoluminescence Emission ........ 32
3.1.3 Low-dose $^{60}Co$ Impact on AlGaN/GaN-based HEMT Devices ........ 38
3.1.4 General Discussion ........ 41
3.2 Minority Carrier Transport Properties in β-$Ga_2O_3$ ........ 42
3.2.1 Prior State of the Art ........ 42
3.2.2 Cathodoluminescence Emission ........ 43
3.2.3 Effect of Surface Etching on β-$Ga_2O_3$ ........ 49
3.2.4 Impact of 10 MeV Proton Irradiation ........ 52
3.2.5 Impact of 1.5 MeV Electron Irradiation ........ 55
3.2.6 Effects of Electron Injection ........ 61
3.2.7 General Discussion ........ 66
3.3 Minority Carrier Transport Properties in InAs/GaSb Type II Strain-Layer Superlattice ........ 68
3.3.1 Prior State of the Art ........ 68
3.3.2 Impact of $^{60}Co$ γ-Radiation ........ 70
CHAPTER IV – CONCLUDING REMARKS & DISCUSSION ........ 76
4.1 Transport properties in β-$Ga_2O_3$ ........ 76
4.1.1 Radiation Impact ........ 77
4.2 Transport Properties of InAs/GaSb Type-II Strain-Layer Superlattice ........ 78
4.2.1 Radiation Impact ........ 78
APPENDIX A – PUBLISHED WORKS ........ 79
APPENDIX B – RELATED ONGOING WORK ........ 82
APPENDIX C – OPTICAL CONSIDERATIONS ........ 87
REFERENCES ........ 89

LIST OF FIGURES

Figure 1. Diagram of p-n junction at rest at thermal equilibrium. ..... 16
Figure 2. Decay process of $^{60}Co$. ..... 17
Figure 3. Experimental EBIC equipment setup. ..... 21
Figure 4. Sample configurations used in EBIC studies. ..... 21
Figure 5. CL experimental schematic. ..... 25
Figure 6. Time-resolved CL signal from GaN. ..... 27
Figure 7. CL spectra of MOCVD-produced GaN. ..... 33
Figure 8. SEM and CL images of GaN produced by MOCVD. ..... 34
Figure 9. Comparison of continuous CL for (a) MOCVD and (b) HVPE-produced GaN. ..... 35
Figure 10. Fitting applied to streak data from GaN at room temperature. ..... 36
Figure 11. Fastest decays found for GaN as a function of temperature. ..... 37
Figure 12. SEM image of AlGaN/GaN HEMT device used for low dose $^{60}Co$ gamma radiation effects. ..... 39
Figure 13. Experimental dependence of minority carrier diffusion length (left axis, closed circles) and activation energy (right axis, open circles) on irradiation dose [55]. ..... 40
Figure 14. Continuous wave CL of β-$Ga_2O_3$ collected at room temperature and 6 kV accelerating voltage presented with Gaussian breakdown. ..... 44
Figure 15. CL emission spectra for Si-doped β-$Ga_2O_3$ by accelerating voltage. ..... 45
Figure 16. CL (top) and SEM (bottom) micrographs of β-$Ga_2O_3$. ..... 46
Figure 17. Streak data for β-$Ga_2O_3$ at room temperature and 10 kV accelerating voltage.**Error! Bookmark not defined.**
Figure 18. EBIC data for (-201)-oriented β-$Ga_2O_3$ reference sample. ..... 51
Figure 19. EBIC data for (-201) oriented β-Ga2O3 after 3 minutes of 400 W of ICP etching. ..... 51
Figure 20. Minority carrier diffusion length in (001) Si-doped β-$Ga_2O_3$ for reference and 10 MeV proton irradiated sample. ..... 54
Figure 21. EBIC data for β-$Ga_2O_3$ for reference and 1.5 MeV electron irradiated sample. ..... 56
Figure 22. EBIC results of L for β-$Ga_2O_3$ for reference and 1.5 MeV electron irradiated samples. ..... 57
Figure 23. Spectral comparison of continuous wave CL for reference and 1.5 MeV electron irradiated β-$Ga_2O_3$. ..... 58
Figure 24. Decay time constant for β-$Ga_2O_3$ as a function of 1.5 MeV electron fluence. ..... 59
Figure 25. Continuous wave CL of MOCVD grown β-$Ga_2O_3$ on c-plane $Al_2O_3$. ..... 62
Figure 26. CL spectra collected for MOCVD grown Si-implanted β-$Ga_2O_3$ on c-plane $Al_2O_3$. ..... 63
Figure 27. Rate measurements of CL intensity decay for MOCVD grown Si-implanted β-$Ga_2O_3$ on c-plane $Al_2O_3$. ..... 65
Figure 28. Schematic of the T2SLS structure. ..... 69
Figure 29. InAs/GaSb T2SLS control-sample EBIC data and linear fit. ..... 72
Figure 30. Temperature dependence of electron diffusion length for InAs/GaSb T2SLS. ..... 73
Figure 31. Electron mobility values for InAs/GaSb. ..... 74
Figure 32. Continuous wave CL spectra temperature comparison for HVPE produced β-$Ga_2O_3$. ..... 83
Figure 33. Presumed electromigration in β-$Ga_2O_3$ as shown by SEM. ..... 84

LIST OF TABLES

Table 1. Material parameters for estimation of electron range. ........ 19
Table 2. Parameters for Gaussian deconvolution of continuous wave CL emission of β-$Ga_2O_3$. ........ 45
Table 3. Material parameters for Si-doped β-$Ga_2O_3$ in response to 10 MeV proton irradiation. ........ 54
Table 4. Material parameters for Si-doped β-$Ga_2O_3$ in response to 1.5 MeV electron irradiation. ........ 59
Table 5. Dispersion grating parameters by instrument. ........ 88

<u>LIST OF ABBREVIATIONS</u>

°C – Degrees Celsius

μ – Carrier Mobility

μSR – Muon-spin Rotation and Relaxation Spectroscopy

2DEG – Two-Dimensional Electron Gas

$^{60}$Co – Atomic Weight 60 Cobalt

A – Ampere

a.u. – Arbitrary Units

Ar – Argon

B – Magnetic Field Intensity

$BCL_3$ – Boron Trichloride

Be – Beryllium

C – Coulomb

CCD – Charge Coupled Device

CL – Cathodoluminescence

D – Diffusivity Constant

DLTS – Deep Level Transient Spectroscopy

$E_a$ – Activation Energy

$E_{a,I}$ – Electron Injection Activation Energy

$E_b$ – Accelerating Voltage

EBIC – Electron Beam-Induced Current

$E_F$ – Fermi Energy

$E_g$ – Bandgap Energy

FWHM – Full Width at Half of Maximum

g – Grams

Ga – Gallium

$Ga_2O_3$ – Gallium Sesquioxide

$Ga_i$ – Gallium Interstitial

GaN – Gallium Nitride

GaSb – Gallium Antimonide

H – Hydrogen

HEMT – High Electron Mobility Transistor

HVPE – Hydride Vapor Phase Epitaxy

$I_{CL}$ – Intensity of Cathodoluminescence

ICP – Inductively Couple Plasma

$I_{EBIC}$ – Magnitude of Electron Beam-Induced Current

InAs – Indium Arsenide

IR – Infrared

J – Joule

K – Kelvin

L – Minority Carrier Diffusion Length

$L_0$ – Asymptotic Minority Carrier Diffusion Length

LED – Light-Emitting Diode

Li – Lithium

LWIR – Long-wave Infrared

m – Meter

$m_c$ – Mass of Charged Particle

MOCVD – Metal-Organic Chemical Vapor Depostion

MWIR – Mid-wave Infrared

N – Nitrogen

Ni – Nickel

$N_i$ – Nitrogen Intersitital

O – Oxygen

PL – Photoluminescence

PMT – Photomultiplier Tube

r – Radius

$R_e$ – Electron Range

RIE – Reactive Ion Etching

s – Seconds

SEM – Scanning Electron Microscope

Si – Silicon

T2SLS – Type II Strain-Layer Superlattice

TL – Thermoluminescence

TRCL – Time-Resolved Cathodoluminescence

TRPL – Time-Resolved Photoluminescence

$t_s$ – Sample Thickness

UV – Ultraviolet

V – Volts

v – Velocity

$V_{Ga}$ – Gallium Vacancy

$V_N$ – Nitrogen Vacancy

$v_s$ – Surface Recombination Velocity

$w_s$ – Sample Width

XRD – X-ray Diffraction

α – Linearization Coefficient

ρ – Mass Density

## PHYSICAL CONSTANTS

| | | |
|---|---|---|
| Å | – Angstrom | $10^{-10}$ m |
| c | – Speed of Light | $2.998 \times 10^{8}$ m/s |
| e | – Fundamental Charge | $1.602 \times 10^{-19}$ C |
| eV | – Electron Volts | $1.602 \times 10^{-19}$ J |
| h | – Planck's Constant | $6.626 \times 10^{-34}$ J·s |
| ħ | – Reduced Planck's Constant | $1.055 \times 10^{-34}$ J·s |
| $k_B$ | – Boltzmann Constant | $8.616 \times 10^{-5}$ eV/K |
| π | – Pi | 3.14159 |

# CHAPTER I – INTRODUCTION

*"It is of great advantage to the student of any subject to read the original memoirs on that subject, for science is always most completely assimilated when it is in the nascent state..."*

–James Clerk Maxwell

## 1.1 Background

Semiconductor devices maintain major advantages in modern technologies including high sensitivity, high-temperature, and high-power applications. In particular, it is common for narrow and wide bandgap-based devices to be deployed in the radiation harsh environment of space. A subset of semiconductor-based devices is utilized for their potential use in viewing the invisible parts of the light spectrum (to humans). Therefore, the behavior of the electronic transport properties of these materials is of practical interest. For this, we turn attention to the impact of radiation on semiconductors with narrow bandgap, InAs/GaSb-based type-II strain layer superlattices (T2SLS), and wide bandgap, GaN & β-$Ga_2O_3$. With a fabrication-tunable bandgap in the mid-to-long wave infrared (IR), the primary and intended application of the T2SLS materials is IR radiation detection. The usefulness of GaN-based devices is well established, with its bandgap of 3.4 eV, it has near UV absorption and emission. While for the β-phase of $Ga_2O_3$, there is a predicted bandgap of ~ 4.8-4.9 eV allowing for solar-blind UV detection. It has been previously demonstrated in GaN that the effects of electron injection can positively impact device functionality and, in fact, restore radiation-damaged devices [1].

With its wide bandgap, β-$Ga_2O_3$ has been gaining attention recently due to the call for high-power and high operating temperature devices. There are many phases of $Ga_2O_3$, namely α-, β-, γ-, δ-, ε-, and κ-, with β- being the most stable and has a monoclinic crystal structure [2]. It is commonly described as a direct bandgap semiconductor with a bandgap of 4.8-4.9 eV, allowing for solar blind ultraviolet detection ($\lambda_{cutoff} \simeq 253$ nm), useful for militaristic/fire detection purposes and scientific research like stellar imaging. Until 2017 β-$Ga_2O_3$ was only available as n-type, but p-type conductivity has been verified, generating new possibilities for bipolar optoelectronic devices and transparent conducting oxide-based devices [3]. The suitability of β-$Ga_2O_3$ for radiation harsh applications depends on its ability to withstand high energy radiation over time.

For the InAs/GaSb T2SLS, bandgap tunability comes from the characteristic number of monolayers (ML) of a given material in a period of the superlattice. For instance, a particular T2SLS structure may consist of 8 ML of InAs followed by 8 ML of GaSb, at ~2.5 Å per ML we may estimate ~ 3.2 nm per period, then repeated to the desired layer thickness. The carrier concentration can be adjusted through doping to be n- or p-type. The tunability of the narrow bandgap of InAs/GaSb-based T2SLS structures makes them attractive candidates for implementation in infrared sensing devices.

Common of these two seemingly unlike materials is the potential deployment in radiation harsh environments. Investigation of the effects of high energy radiation is therefore warranted and necessary to determine material suitability. Gamma irradiation primarily induces ionization defects but may also produce displacement damage. Heavy ions, like protons, more readily

generate displacement defects. Studies of both types of radiation damage are needed to separate the total ionization dose effects from the displacement effects.

Transport properties of minority carriers in bipolar devices are of vital importance. Minority carriers can be thought of as the limiting reactant for the current reaction across a junction. The decay lifetime, $\tau$, describes how long it takes for an excited carrier to decay back to an equilibrium state. The minority carrier diffusion length, L, describes the average distance an excited minority carrier can travel before recombination. It can be useful in gauging how damaged a material or device has become in response to irradiation, even for majority carrier devices.

Investigations into the minority carrier diffusion length and excited carrier lifetime are a subject of import due to their direct links to bipolar device performance. The importance of the temperature dependence of these properties is twofold: first, potential applications may require various temperatures due to environment or for device operation, second, it is possible to infer further information about the occupiable energies in the material. It has been previously determined that the effects of electron injection – sustained forward bias (solid state electron injection), or by electron beam – can have a substantial effect in manipulation of minority carrier diffusion length. It has been assumed that these results extend to minority carrier lifetime, but this has yet to be directly demonstrated.

This chapter begins with a summary of types of luminescence, recombination pathways, and high energy radiation. Followed by structural descriptions of GaN, $\beta$-$Ga_2O_3$ and InAs/GaSb T2SLS along with estimations of available trap states. We then discuss the practical effects of minority carrier diffusion length on bipolar device performance.

### 1.1.1 Types of Recombination & Luminescence

When carriers become excited, they can recombine radiatively or non-radiatively. Non-radiative recombination generally leads to phonon generation, which is not so easily measured. Radiative recombination occurs when an excited charge decays into a lower energy state, the transition energy is emitted as a photon. For direct bandgap semiconductors, the emitted photon energy is near or equivalent to that of the bandgap. It is possible for an excited charge to decay into a localized trap state in the forbidden band. Trap-assisted recombination, known as Shockley-Reed-Hall recombination, can lead to wider spectral emission at wavelengths representative of less than bandgap energy. Traps can remain occupied for varying lengths of time depending on numerous factors including the origin (defect type) and local temperature [4]. It is necessary to take note of the timescales of luminescence. The regimes of luminescence are generally divided into *fluorescence* for $\tau$ shorter than 10 ns, and *phosphorescence* with $\tau$ longer than 10 ns. Thermally stimulated emission is referred to as thermoluminescence (TL), which is the release of trapped charges due to thermal agitation. The decay times for TL processes can be of extremely high order ~ years or better [4].

### 1.1.2 Types of High Energy Radiation

Throughout the manuscript, various forms of radiation are applied to materials. These high energy radiations can be found in space, generally referred to as *cosmic rays* of yet undetermined origin. Such high-energy particle radiation can be found to be concentrated in the

van Allen radiation belts or upon elevated solar activity [5]. The radiation consists of (in order of mass, lowest to highest) gamma, electron, proton, and alpha radiation.

*Gamma* (γ) radiation consist of high energy (5 keV < $E_\gamma$ < 8 MeV).The term *gamma-ray* has been conventionally defined as radiation emitted from a nucleic reaction in a radioactive decay process. It is possible for x-rays to carry the same energy and are therefore indistinguishable from gamma-rays if the source is unknown. Therefore, the results of gamma irradiation in fact apply to high-energy photons of similar fluence and energy, and are not specific to photons of a specific source. Hence, throughout this text, *gamma-ray* will refer to photons with energy in the range 5 keV < $E_\gamma$ < 8 MeV. The types of defects generated by gamma-rays are displacement and ionization defects, and tend to generate Compton electrons, internally flooding the material with high energy electrons. Due to the small cross-section of these photons, the dose from gamma-rays is more uniform throughout a volume.

*Electron* ($e^-$) radiation consists of high energy electrons ($E_e$ > 100 keV). High energy electrons native to various Earth orbits carry a range of energies exceeding 2 MeV and reaching relativistic speeds due to the small mass of electrons, $m_e$. Electron irradiation can lead to displacement defects and ionization defects. The proportion of which types of defects generated depends on the incoming energy. Energetic electrons found in orbit and those from cyclotron differ only in source and energy. The electrons used in electron irradiation are indistinguishable from any other electron.

*Proton* ($p^+$) radiation consists of high energy protons ($E_p$ > 100 keV). With a particle mass ~1,833 times larger than that of electron, these ions can generate displacement defects in materials. Ionization defects can be generated also, but to a lesser degree due to the inflated

particle mass. The effective penetration depth of proton radiation depends on energy but is not as uniform as that of gamma or electron irradiation.

*Alpha* (α) radiation consists of high energy alpha particles ($E_\alpha$ > 100 keV). Alpha particles are bosons and can be described as fully ionized Helium nuclei. Most natural sources of alpha decay release particles in the 3 to 7 MeV energy range. With nearly four times the mass of a proton, the magnitude of achievable velocities for alpha particles is substantially lower than for other particle radiations. As such, high energy alpha radiation tends to generate displacement defects at a reduced skin depth.

To observe the impact of these radiations, artificial sources of radiation have been employed throughout the manuscript. Aside from energy and source, these radiations are presumably indistinguishable from their cosmic counterparts.

## 1.2 Structural overview of GaN, β-$Ga_2O_3$ and InAs/GaSb (T2SLS)

Semiconductor elements are commonly crystalline, and their crystal structure can be of significant interest. It has been demonstrated that radiation hardness of materials depends roughly on inverse lattice constant [6]. Crystallographic anisotropy can lead to anisotropy of other characteristics like electric or thermal conduction, and influence photo absorption or emission polarities.

### *1.2.1 Gallium Nitride*

Gallium nitride, GaN, is a III-V semiconductor which has been used in devices since the mid-1990's, and is commonly employed in light-emitting diodes (LEDs) and AlGaN/GaN-based

devices, such as high electron mobility transistors (HEMTs). GaN can be produced by several methods including molecular beam epitaxy (MBE), hydride vapor phase epitaxy (HVPE), and metal organic chemical vapor deposition (MOCVD). The crystallographic structure of GaN has been well-characterized and is known to be wurtzite with tetrahedral coordination. The lattice constants for GaN are a = 3.186 Å, and c = 5.186 Å.

The electronic bandgap of GaN is about 3.4 eV, making it an ideal material for producing near-UV LEDs and sensors. The percent content of aluminum vs gallium in $Al_xGa_{1-x}N$ predictably controls the bandgap linearly from 3.4 (for x = 0) to 6.2 (for x = 1.0) eV [7]. GaN is naturally n-type, but can be made p-type via doping.

### *1.2.2 Gallium Sesquioxide*

The β- phase of gallium sesquioxide, β-$Ga_2O_3$, is the most thermally stable. Annealing up to 750 – 900 °C of other phases of $Ga_2O_3$ lead to formation of β-$Ga_2O_3$ on cooling. The thermal stability of the β- phase allows for production via melt crystallization or vapor phase epitaxial methods. The crystallographic structure is monoclinic in nature and resides in the C2/m space group as verified by X-ray diffraction (XRD) techniques [2]. A unit cell has two inequivalent Ga sites, tetrahedrally coordinated Ga(I) and octahedrally coordinated Ga(II), and three inequivalent O sites, O(I), O(II), and O(III). The lattice constants for β-$Ga_2O_3$ are a = 12.214, b = 3.0371, and c = 5.7981 Å.

With a nominal bandgap of 4.8-4.9 eV, is generally transparent with a slight bluish hue generally depending on carrier concentration. β- has been investigated more frequently than

other phases, and depending on defect type and concentration, and unintentional dopant levels, can be produced as n-type, or p-type as recently demonstrated [3].

### *1.2.3 InAs/GaSb Type II Strain-Layer Superlattice*

The superlattice is a composite structure composed of repeating periods of binary material layers. Both Indium arsenide, InAs, and gallium antimonide have zincblende crystal structure while the former has a bandgap of 0.354 eV and lattice constant a = 6.058 Å while the latter has a bandgap of 0.726 eV and lattice constant of a = 6.1 Å. A mismatch of Fermi levels in InAs and GaSb is utilized to create a pseudo quantum well structure, which is repeated numerous times. Similarities in the crystal structure and lattice constants of InAs and GaSb allow for strain compensation or enhancement depending on terminating atoms in the binary pairs during production [8]. The low number of MLs typically used in a single period (1-20 ML / period) prevents the binaries from attaining their bulk characteristics and instead forms a composite material.

The bandgaps of the T2SLS has been successfully demonstrated to be production-tunable from 3-30 μm, including two of the terrestrially transparent spectral windows, mid-wave infrared (MWIR) from 3-5 μm, and long-wave infrared (LWIR) from 8-12 μm [9]. Their layered structure forces an anisotropy, due to the surface roughness and electronic differences of the InAs and GaSb layers, along the growth direction.

## 1.3 Trap States in GaN, β-$Ga_2O_3$, and InAs/GaSb T2SLS

With energy levels within the forbidden band, some allowable states act as carrier traps. Trap states can have origins related to defects in the material (vacancies, interstitials, antisites, or complexes like Frenkel pairs) which can be native or induced, or the presence of impurity atoms. They can become occupied and remain so for extremely long times or they may evacuate instantly and can vary depending on environmental factors like temperature [4]. The occupation of trap states influences local electronic properties may effectively screen recombination lifetime.

### *1.3.1 Activation Energy, $E_a$*

When a charge trapping site becomes occupied, it may escape its binding through thermal agitation. The binding energy or affinity to hold charge can be quantified by observing the rate at which these traps become occupied or evacuated as a function of temperature. The activation energy, $E_a$, then describes the energy distance from a band [10].

## 1.4 Cathodoluminescence Spectroscopy

Cathodoluminescence (CL) is just what it sounds like, luminescence of a cathode material where the cathode material is experimentally varied. An electron beam is used to excite carriers with excessive energy to activate recombination mechanisms, some of which are radiative. This is similar to photoluminescence technique (PL) which uses a light source to excite charges. PL versus CL has some advantages and disadvantages for material characterization. The most concerning comparisons are generally: (1) the light source cannot be focused smaller than an

electron beam, (2) a light source is limited to the energy of the light being injected, and (3) the PL method allows for determination of spectral absorption.

The charges which radiatively recombine emit light whose energy is related to the energetically favorable recombination pathway(s) present in the material. CL-stimulated light emission is characteristic to the material and can be spectrally separated using spectrometer or monochromator, and spatially separated using pseudo-point excitation. In general, direct bandgap materials will emit at their bandgap energy while indirect bandgap materials may emit at or below their bandgap energies.

The technique can therefore also be used to determine the spatial distribution of materials, which makes it particularly useful (and lucrative) for characterization of material production methods and device failure analysis [11].

This reveals details about carrier recombination behavior and can yield information about material composition [11], trap activation energy [12-14], defect density [15, 16], and plasmonic mode dispersion [17, 18]. The spatial resolution of this technique is limited by minority carrier diffusion length and size of generation volume [19, 20]. The minority carrier diffusion length can be determined by the EBIC technique [21-23].

#### *1.4.1 Decay Lifetime, τ*

The addition of time resolution to the cathodoluminescence technique allows for direct measurement of spectral decay, which can reveal radiative recombination lifetime, $\tau$, [24] and the presence of stress and strain [25]. Decay can be observed directly using a time-dependent (or pulsed) electron beam or light beam excitation, these techniques are referred to specifically

as time-resolved cathodoluminescence (TRCL) and time-resolved photoluminescence (TRPL) respectively. The decay is generally exponential is nature and can have multiple components. The general form of intensity decay is

$$I(t) = \sum_{i=1}^{N} I_i \exp(t/\tau_i) \tag{1}$$

where I is intensity, N is the number of separable emission components, and t is time. $N = 1$ is most commonly observed, and indicative of a single dominant radiative recombination behavior. An example is Shockley-Reed-Hall, trap assisted, recombination which uses interband trap states as stepping stones for excited carriers to reach their low energy equilibrium state. Observing equation (1) for decay shows that $\tau_i$ describes the intensity decay of process *i* to the value 1/e, similar to capacitive behavior.

### 1.5 Minority Carrier Diffusion Length Effect on Device Performance

Diffusion occurs upon spatial variation of the carrier concentration in a semiconductor material. A diffusion current occurs when carriers migrate from areas of high to low concentration. The minority carrier diffusion length, L, in semiconductors describes the statistical distance an excited carrier will travel in a given direction before recombination. The diffusion length can be related to lifetime by

$$L = \sqrt{D\tau} \tag{2}$$

where D is the diffusion coefficient, which is related to the mobility by the Einstein relation

$$D = \mu k_B T/e \tag{3}$$

where $\mu$ is the carrier mobility, $k_B$ is the Boltzmann constant, T is the temperature in Kelvin, and e is the fundamental charge. A myriad of practical device performance benchmarks depend on L, including dark current and quantum efficiency. The behavior of minority carriers is of interest especially for bipolar devices, since minority carriers are the limiting reactant in current across a junction.

Once excited, the carriers will diffuse according to charge concentration and local electric field. A particular instance of an intrinsic electric field in a semiconductor material is at or near a junction – p-n junction, Schottky barrier, or surface-vacuum interface. The built-in electric field draws in excited charges, the junction collects them, and they can be measured as current. The current collected can then be used to determine the diffusion length from excited charge position. Since the electric field is always oriented such that minority carriers will be collected, this current is related to the minority carrier diffusion length, L. Currents generated by electron beam are known as electron beam-induced current (EBIC). EBIC analysis can be instrumental in determination of L in a given material.

## 1.6 Dissertation Outline

To determine the suitability of materials for radiation harsh environments, studies of the effects of high energy radiation are crucial to the evolution of materials toward full implementation in mature device technologies. Further, it is necessary to investigate the effects of electron injection for the practical purpose of possibly developing radiation degradation mitigation strategies. The effects of various high energy radiations will be investigated to show the effects of the induced damage for AlGaN/GaN-based HEMT devices, Si-doped $\beta$-$Ga_2O_3$, and

an 8/8 ML ratio InAs/GaSb T2SLS. Temperature-dependent measurements of L and $\tau$ will reveal shallow interband trap activation energy, $E_a$, for $\beta$-$Ga_2O_3$ which may be characteristic of silicon (Si) or hydrogen (H) inclusions.

Chapter two will describe the experimental techniques used to evaluate the material properties (EBIC, CL, and TRCL), in response to stimuli (electron injection or irradiation). The theoretical model used to describe EBIC will be presented with indications of the conditions of validity for the determination of L and thermal $E_a$. The CL techniques for determination of recombination behavior and trap state thermal activation energy are presented.

Chapter three presents experimental results including sample pedigree and experimental conditions. The primary focus of this chapter is the impact of temperature and various irradiations on the minority carrier transport properties in $\beta$-$Ga_2O_3$ and the InAs/GaSb T2SLS.

The fourth and final chapter discusses the results of the experiments and reviews their implications on device performance for the future of $\beta$-$Ga_2O_3$ and InAs/GaSb T2SLS materials.

# CHAPTER II – EXPERIMENTAL SETUP & TECHNIQUE

*"Science walks forward on two feet, namely theory and experiment."*

–Robert Milikan

## 2.1 Sample Characterization

In this chapter the experimental procedures and conditions are reported including the experimental setup and techniques used for sample characterization. The major techniques utilized in this section include EBIC and CL. The EBIC technique yields information about sample diffusive properties. The CL technique allows the determination of charge recombination behavior including the intensity spectrum and decay lifetime. These techniques will be used to determine the impact(s) of specific irradiation on carrier transport properties and trap activation energies.

Complementary techniques will also be used to characterize samples. Some properties must generally be determined via complementary methods other than those mentioned here, such as Hall measurements to find carrier type and density, XRD to determine crystallinity, quality, and orientation, and spectral photoresponse to determine spectral absorption.

### *2.1.1 Semiconductor Junctions*

A semiconductor junction is created when there is a significant gradient in charge concentration. This can result from the joining of p- and n-type semiconductor materials (p-n junction), application of metal to a semiconductor (Schottky barrier), and even the interface

between semiconductor and vacuum. This is the description of a bipolar device, meaning both polarities of carriers are used for current conduction.

At thermal equilibrium we find a non-zero electric field at material junctions. This occurs due to the differing charge concentrations of the junction materials. Electrostatic attraction causes electrons (holes) from the n-type (p-type) material to diffuse into the p-type (n-type) material. This charge separation produces an electric field directed from the n- to the p-type material. This causes a displacement of charge which leads to a gradient in charge concentration, therefore, at thermal equilibrium there must be a balance between the drift of charges across the boundary and the diffusion of charges due to the charge concentration gradient.

The displacement of the charges at the junction leads to a low excess carrier density known as the depletion region, or space-charge region, where the free carrier concentration is very low. In the bulk, the valence and conduction band energy levels are constant, but, near the junction, the bands are noticeably *bent* due to the matching of the Fermi level energy. The Fermi energy is the highest energy level which electrons will occupy at absolute zero. An example of a p-n junction is presented in Figure 1.

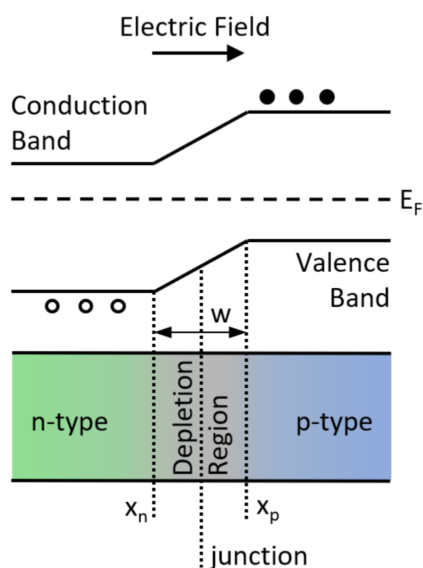


Figure 1. Diagram of p-n junction at rest at thermal equilibrium. The top portion illustrates the energy band behavior, with excited electrons (filled circles) and holes (open circles), the electric field direction, Fermi level, and depletion region width are indicated. The bottom portion illustrates the material junction cross-section.

### 2.2 Sample Irradiation

Gamma irradiation is performed by controlled exposure to a $^{60}$Co source at room temperature in an inert nitrogen environment. Gamma radiation from $^{60}$Co decay has two discreet photon energies above 1 MeV, the decay process is depicted in Figure 2. The probability of the lower energy beta decay is more than 99% more likely than the higher energy beta decay. This means that the populations of the two energies 1.17 and 1.33 MeV are nearly equal. The advantages for gamma-irradiation are the homogeneity of defect distribution, lack of secondary radiation enabling immediate handling, and low irradiation cost.

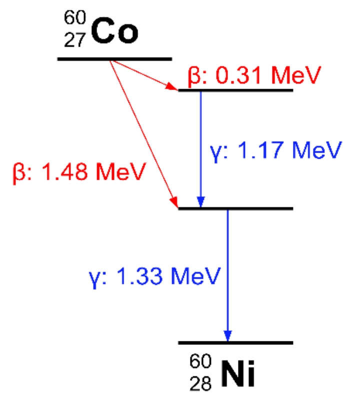


Figure 2. Decay process of $^{60}$Co. The transmutation into Ni occurs via two possible beta particle emissions (red) leading to two distinct gamma-ray emissions (blue).

A study performed by the Naval Research Laboratory showed that for InP, GaAs, and Si based solar cells, the effects of electron and gamma-irradiation were equivalent [26]. Gamma-irradiation produces Compton electrons with ~ 600 keV mean energy, effectively internally irradiating the material with energetic electrons. This suggests a possible equivalence of gamma and electron irradiation for defect formation, and it allows advantageous use gamma-rays to simulate electron irradiation.

Particle irradiation is performed using a cyclotron to generate a high-energy charged particle beam. A cyclotron is a particle accelerator which uses the Lorentz force to accelerate charged particles to high speeds. In the absence of an electric field component, electrons moving perpendicular to magnetic fields will exhibit uniform circular motion. The magnetic field is omitted from a slab which lies parallel to the magnetic field. In this region, after exiting the magnetic field, an electric field is applied to accelerate the charged particles before entering another magnetic field region. The circular motion radius enlarges each time an acceleration is applied in the magnetically blank region, consistent with its higher velocity

$$r = m_c v / eB \quad (4)$$

where r is radius, $m_c$ is mass of particle, v is particle velocity, and B is the magnitude of the magnetic field. Using this relatively simple method, high energies can be imparted to charged particles. Charged particles can be accelerated to relativistic speeds and a beam can be sustained. This method is used for electron and proton irradiation.

### 2.3 Generation Volume & Electron Range

The characterization methods EBIC and CL which follow utilize an electron beam from a scanning electron microscope (SEM) source. An electron beam can be focused to have a nominal radius of nearly 5 nm, which is the among the chief limiting factors for SEM image resolution. For EBIC and CL, the corollary limiting factor for resolution for these techniques is the size of the volume of excited minority carriers due to SEM beam influence. This volume is referred to as the generation volume. Ultimately, the shape of the generation volume depends on the SEM accelerating voltage, $E_b$, as well as the sample material density, ρ, present scattering anisotropy, and surface recombination. However, it can be roughly estimated with a fourth order polynomial

$$g(z) = 0.6 + 6.21z - 12.40z^2 + 5.69z^3 \quad (5)$$

where z is distance below the surface-vacuum interface normalized to electron range. The value of g describes the radially symmetric normalized generation volume carrier density as a function of normalized depth.

The depth of the influence of the electron beam is known as the electron range, $R_e$. In most cases it is sufficient to estimate the width of the generation volume to be ~ ½ $R_e$ [27]. It has

been shown in numerous publications that approximate $R_e$ is expressible in a closed form with relative accuracy. The Grün expression is given by

$$R_e = 45.7 \frac{E_b^{1.75}}{\rho} \qquad (6)$$

Though, approximations throughout the derivations of $R_e$ require the use of slightly different expressions for ranges of accelerating voltage, for beam energies below 5 keV, these semi-empirical methods tend to fail by more than 10 % to agree with Monte-Carlo simulation results, which are generally regarded as more accurate. The expression by Grün from 1957 tends to be the simplest and most accurate of the available expressions from 10 to 30 keV [28].

The material parameters used throughout the manuscript are listed in Table 1.

Table 1. Material parameters for estimation of electron range.

| Material Parameter | GaN | β-$Ga_2O_3$ | InAs | GaSb |
|---|---|---|---|---|
| Mass density, ρ ($g/cm^3$) | 6.15 | 5.88 | 5.67 | 5.614 |
| Atomic number, $Z_{avg}$ | 19 | 17.2 | 41 | 41 |
| Molar mass, $A_{avg}$ (g/mol) | 41.87 | 37.49 | 94.91 | 95.75 |

### 2.4 Electron Beam-Induced Current (EBIC)

The EBIC method has been employed for greater than 40 years for determination of L in semiconductor materials [23, 29, 30]. Though there is still some debate as to the accuracy of the expressions used to determine L from EBIC data [27, 31, 32]. Using an electron beam, minority carriers become excited which can diffuse to a nearby junction, become accelerated across the junction, and measured as EBIC.

There are several variations on the EBIC method for determination of L. For instance, the works of Wu & Wittry where Schottky barriers are bombarded with an electron beam and the voltage was varied. By estimating the depletion region depth and the shape of the generation volume and directly measuring the beam current, the value of L is determined by observing the collection efficiency as a function of voltage. This method can be very accurate [31], but require excessive voltages and an accurate measurement of the beam current [33]. Instead turn to the work of Berz & Kuiken, which involves measuring the current as a function of beam distance from the junction [29]. The population of carriers which reach the junction for collection reduces with increasing distance of the electron beam from the junction.

### *2.4.1 EBIC Setup*

Measurements were carried out *in-situ* in a Philips XL-30 TMP SEM. The experimental EBIC schematic is displayed in Figure 3. Samples are mounted on an insulator to isolate electrical signals from the microscope hardware. The insulator is attached to a temperature-controlled stage with available temperature control from 80 to 393 K, as measured by an integrated platinum resistance thermometer with a 0.5 K accuracy.

One of the electrical contacts of the sample is connected to a Stanford Research Systems SR570 current pre-amplifier with the second contact connected to an external electrical ground. Because the beam currents of SEM are typically on the order of $10^{-9}$ A, EBIC signals from the sample can be of similar order. The current pre-amplifier allows for low level sensitivity and amplifies the small generated EBIC. The current pre-amplifier output is connected to a Keithley 2000 Multimeter which digitizes a detected voltage for collection by a Dell computer using

LabView software. The voltage can then be converted to current by multiplying the gain of the amplifier in units A/V.

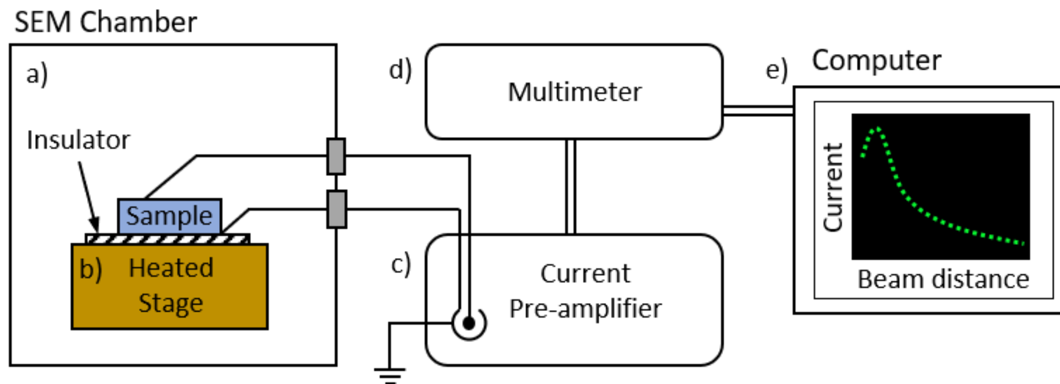


Figure 3. Experimental EBIC equipment setup. The sample is mounted inside the SEM chamber (a) on a temperature-controlled stage (b) and electrically insulated. The signal is sent to a current pre-amplifier (c) and digitized by the multimeter (d). Finally, the data is collected by a lab computer (e).

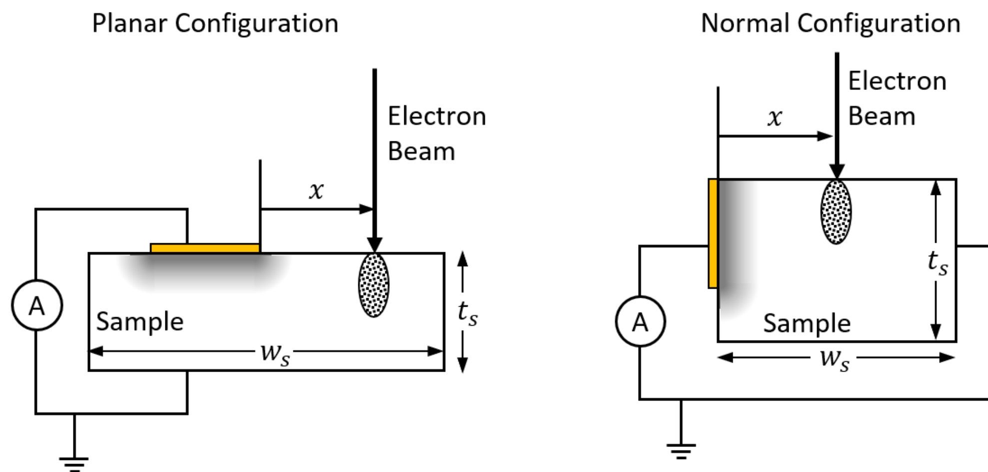


Figure 4. Sample configurations used in EBIC studies. A cross sectional side view of the planar configuration (left) and the normal configuration (right) are presented with Schottky barrier junctions (yellow). The depletion region is exaggerated and shown in gray. The beam-to-junction distance x, and the sample width & thickness are indicated as $w_s$ and $t_s$, respectively.

The sample can be oriented in various configurations to allow for meaningful data collection. The configurations used here are presented in Figure 4 for Schottky barriers but are generalizable to p-n junctions as well.

*2.4.2 Determination of L*

Many analytical derivations exist for descriptions of EBIC as a function of distance. Following the efforts of Berz & Kuiken [29] derived in 1975 to the more recent work of Kurniawan *et al*. [22] in 2006. The general expression for the collected current is

$$I_{EBIC}(x) = I_0 x^{\alpha} \exp(-x/L) \tag{7}$$

where I is the current scaling constant, x is the beam-to-junction distance, and α is the linearization coefficient related to the *surface recombination velocity*, $v_s$. The surface recombination velocity is the dot product of the diffusion current with the surface normal. Its impact depends on the charge affinity of the sample (the strength of the field at the surface-vacuum junction) as compared to the beam voltage (size of the generation volume), and the collection configuration used (see Figure 4). The range of α in the planar configuration Figure 4 (left) is given by [22]

$$\alpha = \begin{cases} -1.5 \\ -0.5 \end{cases}, \qquad v_s = \begin{cases} \infty \\ 0 \end{cases} \tag{8}$$

and for the normal configuration Figure 4 (right)

$$\alpha = \begin{cases} -0.5 \\ 0 \end{cases}, \qquad v_s = \begin{cases} \infty \\ 0 \end{cases} \tag{9}$$

The value estimated for α should be such that linearizes the output of the expression $\ln(I_{EBIC} x^{-\alpha})$ since, from (6) it is evident that

$$\ln(I_{EBIC}x^{-\alpha}) = -x/L + \ln(I_0) \quad (10)$$

Once linearized, the slope of the data can be extracted and is theoretically -1/L. Of course, this method has some caveats from the mathematical treatment of the problem which should be included in any EBIC analysis. The regions of validity for equation (7) will be discussed in the following section.

### *2.4.3 Validity of the Method*

Due mainly to the influence of the generation volume, certain conditions must be satisfied before claiming validity of equation (7). To begin, the sample thickness, $t_s$, and the sample width, $w_s$, should be greater than several times L and $R_e$ ($t_s$, $w_s$ >> L, $R_e$) [34]. The lateral radius of the generation volume should not be greater than 4L (½ $R_e$ < 4) [27]. The beam to junction distance should be greater than 2L [29]. The primary limit of the technique, however, is the experimental difficulty of measuring vanishingly small currents.

### *2.4.4 Thermal Activation Energy of Diffusion*

The trap thermal activation energy of diffusion can be determined by measuring the value of L as a function of temperature. The following relation describes L as a function of temperature

$$L(T) = L_0 \exp\left(-\frac{E_a}{2k_BT}\right) \quad (11)$$

where $L_0$ is the asymptotic L, $E_a$ is thermal activation energy, $k_B$ is the Boltzmann constant, and T is temperature. A target temperature is maintained for a minimum of 5 minutes before any measurement data are collected.

## 2.5 Cathodoluminescence Technique

Cathodoluminescence refers to the phenomenon in which carriers are excited by an electron beam and their radiative recombination behavior observed. The energy supplied by the electron beam is sufficient to excite free carriers which can recombine radiatively in semiconductors. The emission can be captured by optical components and dispersed to produce a spectrum. The spectrum is characteristic to the recombination pathways available in a given material. Direct bandgap materials tend to emit strongly at or near their bandgap energy. For indirect bangap materials there may be more energetically favorable pathways, and thus tend to emit below their bandgap energy.

### *2.5.1 CL Setup*

CL measurements were collected *in-situ* with an SEM, there are two CL capable SEMs used here, a Philips XL-30 SEM and an Attolight Alalin 4027 Chronos. The basic CL setup is presented in Figure 5. The XL-30 SEM is equipped with a Gatan MonoCL3, which collects light with a parabolic mirror and uses a blazed grating-based Czerny-Turner style monochromator. The grating has 1200 grooves/mm blazed at 500 nm. The monochromated signal outputs to a Hamamatsu photomultiplier tube (PMT), sensitive from 180 to 850 nm. The temperature range used for experiments in the XL-30 is restricted to vary between 80 to 393 K using liquid nitrogen cooling and resistive Joulean heating. The available acceleration voltages range from 3 to 30 kV. The electron beam in the XL-30 SEM cannot be pulsed at speeds significantly fast enough to probe

the temporal recombination behavior, and therefore operates in the continuous mode only (see below).

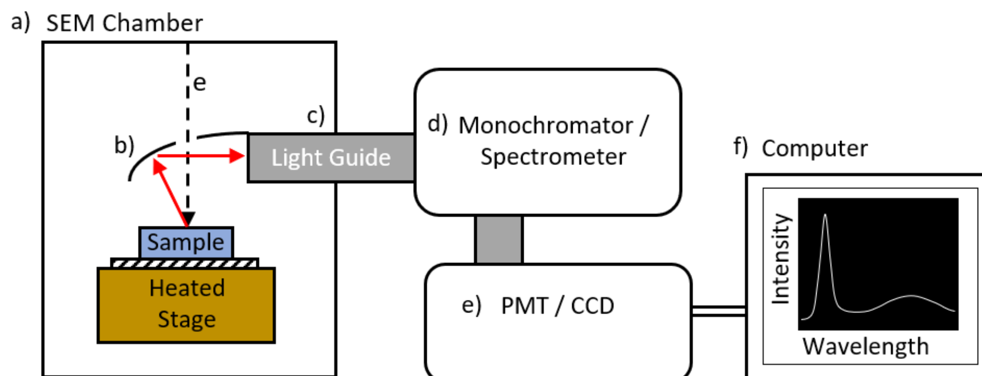


Figure 5. CL experimental schematic. The emitted light is collected by a curved mirror (b) and channeled into a light guide (c), the light is then dispersed by a monochromator or spectrometer (d). The spectrally separated light is fed to a PMT or CCD device (e) which collects and transmits the signal to a nearby computer (f).

Unlike the XL-30, the Attolight SEM was designed specifically for CL collection. The currents available are much higher than that found in other conventional SEM, allowing for higher population of CL emission. However, the beam acceleration voltage is restricted to below 10 kV. It is outfitted with a pseudo-parabolic mirror optimized for wider field of view collection than parabolic mirrors. The Czerny-Turner style spectrometer uses a blazed grating with 150 grooves/mm at 500 nm. The spectrometer outputs to an Andor brand Newton 920 charge coupled device (CCD) for continuous CL collection from 200 to 1100 nm and an Optronis Streak Camera for pulsed mode TRCL collection sensitive from 180 to 850 nm with a minimum temporal resolution of 2.5 ps. The sample stage can be cooled using liquid helium to approximately 10 K, however, the hardware necessary for such an extremely low temperature prevents from achieving temperatures higher than 320 K.

#### 2.5.1.1 Continuous wave excitation

Both SEMs are capable of collecting continuous wave CL signals, since this is the standard operating mode and can be used for CL emission of fluorophores and phosphors. For this mode, the beam is kept on, and data is collected over a given dwell time. The dwell time can be adjusted but is on the order of $10^{-6}$ to $10^{0}$ s, and should generally be at equilibrium for direct bandgap semiconductor samples. Exceptions include phosphorescent materials with lifetimes greater than 10 ns.

The continuous wave mode is useful for extracting spatial CL information which can be used to determine certain defect concentrations, and material distribution. The data can be easily collected and used to produce a CL spectral map. The map production relies on the assumption that the only light emission is coming from the generation volume, and no excessive plasmon propagation or secondary sources are present. With this, the SEM records CL data and assigns position data to it based on the electron beam position.

#### 2.5.1.2 Pulsed mode excitation

The Alalin SEM is equipped with a OneFive high intensity ~250 nm laser which is focused onto the electron gun emission tip and pulsed to generate short electron pulses via the photoelectric effect. The laser is active for approximately 8 fs at a frequency of 80 MHz (period = 12.5 ns), and generates short electron pulses of about 5-8 ps. The pulsed mode excitation is not

ideal for CL map production or imaging because the beam spends the majority of its time in the off-state (8 ps pulse with a 12.5 ns repetition period). The streak camera is synchronized at 80 MHz and disperses signals by wavelength and time. The sample emission due to a single pulse is not generally populated enough to be sufficient for measurement, to compensate, the streak camera accepts multiple frames and stacks them. The intensity should be integrated around the peak of interest, equation (1) can then be applied, and the lifetime extracted.

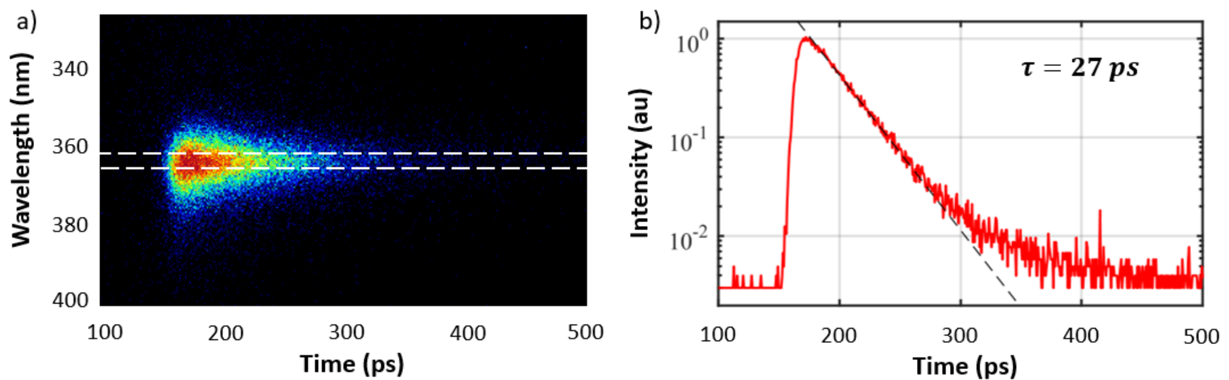


Figure 6. Time-resolved CL signal from GaN. The streak data from GaN is presented (a) with intensity scaling from blue (low) to red (high). The intensity is wavelength integrated over a short bandwidth around the peak (white dashed lines) and presented in red (b). Fitting was accomplished using equation 1 with N = 1 (black dashed line) and estimated a lifetime of 27 ps.

### *2.5.2 Limitations of the Technique*

The CL technique can be used to determine the bandgap energy in direct bandgap materials. For composite materials like $Al_xGa_{1-x}N$, the bandgap is tunable and dependent on the concentration of aluminum to gallium. The bandgap energy can be extracted and determine the uniformity of constituent distribution. This capacity is limited by the difference in material luminescence and bandgap energy differences imposed.

Limitations on the Attolight equipment, namely the frequency of pulse generation, prevent the collection of phosphorescent lifetimes (τ > $10^{-9}$ s), since they exceed the laser pulse and streak camera repetition rate.

2.5.2.1 Cathodoluminescence resolution

Assuming the SEM is focused properly, the primary factor limiting spatial data resolution is the lateral extent of the generation volume and the diffusion length of excited free carriers. There is also the possibility of absorption of the emitted light followed by a re-emission, which would enlarge the luminescing region. This generally would not occur in indirect bandgap materials.

The spectral resolution is limited primarily by the optical components and the spectrometer (or monochromator) grating used for dispersion. In the detectable wavelength ranges, emission peaks can be resolved on the order of ~3 nm full width at half maximum (FWHM) bandwidth.

### *2.5.3 Thermal Activation Energy of Luminescence*

The trap thermal activation energy of luminescence can be determined by measuring the intensity as a function of temperature. The following relation describes CL intensity, $I_{CL}$, as a function of temperature

$$I_{CL}(T) = \frac{A}{\left(1 + Bexp\left(-\frac{E_a}{k_B T}\right)\right)} \qquad (12)$$

where A and B are scaling constants, $E_a$ is thermal activation energy, $k_B$ is the Boltzmann constant, and T is temperature. A target temperature is maintained for a minimum of 5 minutes before any measurement data are collected. Equilibrium CL intensity is proportional to the rate of carrier recombination, and inversely proportional to the minority carrier lifetime.

Under continuous stationary electron beam excitation, local traps begin to become occupied and alter the intensity of CL intensity. This implies a time dependence on the intensity of CL under a continuous electron beam excitation. Since $I_{CL}$ is inversely proportional to minority carrier lifetime, combining equation (2) with equation (11) one finds [35]

$$I_{CL}^{-1} \propto \tau = \frac{L_0^2}{D} \exp\left(-\frac{E_a}{k_B T}\right) \tag{13}$$

which implies a time dependence on the value of $L_0$ under continuous electron beam excitation. The rate of increase in $L_0$ can be inferred then from observing the inverse root intensity of CL as a function of time and temperature. The rate, R, of change is proportional to

$$R(T) = R_0 \exp\left(\frac{\Delta E_a}{k_B T}\right) \tag{14}$$

where $R_0$ is a constant. Rectifying equation (13) and equation (14) demands that

$$\Delta E_a = E_{a,I} - E_a/2 \tag{15}$$

where $E_{a,I}$ is the characteristic electron injection activation energy [36]. The only implicit assumption is that the trap levels do not appreciably begin to saturate during measurement – that the rate of carriers becoming occupied by traps is not equal to the rate of carriers escaping their trap.

# CHAPTER III – RESULTS & DISCUSSION

*"An experiment is a question which science poses to Nature, and a measurement is the recording of Nature's answer."*

–Max Planck

## 3.1 Minority Carrier Transport Properties in Gallium Nitride

### *3.1.1 Prior State of the Art*[1]

Investigations of the radiation effects in AlGaN/GaN-based devices employing energetic protons have consistently reported that proton-irradiation results in a decrease in two-dimensional electron gas (2DEG) sheet carrier concentration and a positive threshold voltage shift with increasing proton dose [38-41]. Negative threshold voltage shifts and increase in 2DEG sheet concentration have been observed in AlGaN/GaN HEMT structures exposed to 1-MeV neutron irradiation with fluences up to 2.5 x $10^{15}$ $cm^{-2}$ [42]. In contrast to the behavior observed in proton-irradiated HEMTs, negative threshold voltage shifts are also observed in gamma-irradiated devices [43-45].

---

[1] Portions of § 3.1.1 Prior State of the Art are published in Electrochemical Society Journal of Solid State Science and Technology, Jonathan Lee, Elena Flitsiyan, Leonid Chernyak, Joseph Salzman and Boris Meyler. *Effects of Gamma Irradiation on AlGaN-Based High Electron Mobility Transistors,* **6**, Published September 22, 2017.

According to a tight-binding model analysis on $Al_xGa_{1-x}N$, nitrogen vacancies, $V_N$, can behave as shallow donors in GaN and deep traps in AlN [46, 47]. The model predicts that $V_N$ will present as s-like, or $A_1$, donor levels and p-like, or $T_2$, levels. For Al concentrations from $0 < x < 0.5$, the $T_2$ level remains above the conduction band edge while the $A_1$ level remains in the forbidden band. While nitrogen interstitials, $N_i$, form deeper acceptor levels near 1 eV below the conduction band edge. For gallium vacancies, $V_{Ga}$, a half-occupied p-like $T_2$ level forms just above the valence band, which can act as a trap for both electrons and holes. When charged, $V_{Ga}$ can form acceptor states near 1 eV above the valence band, while gallium interstitials, $Ga_i$, form donor levels with 3+/2+ charge transition level located near 1 eV below the conduction band [48, 49].

Energy levels induced by $^{60}Co$ gamma irradiation have been detected in GaN by deep level transient spectroscopy (DLTS). The energy levels of the irradiation induced defects were found at 89 and 132 meV. The lower energy was related to $V_N$ defects while the higher energy was possibly due to coupled neighboring defects [50]. The coupling of an interstitial and nearby vacancy is known as a Frenkel pair. These defects have been observed experimentally in GaN after being subjected to 0.7-1.0 MeV electron irradiation [51]. The Hall mobility was observed to decrease after irradiation with $5 \times 10^{16}$ 1 MeV electrons/cm$^2$, and introduced new donors with ionization energy of 0.06 eV [51]. However, there was only a slight change in majority carrier concentration. This is significant because $V_{Ga}$ acts as a triple acceptor in n-type GaN, while $Ga_i$ is a single donor. Therefore, with Ga lattice Frenkel pairs there is a marked change in majority carrier concentration. While for Frenkel pairs generated in the N lattice, $V_N$ tend to behave as shallow donors, and $N_i$ as deep acceptors yielding no net change in carrier density. The effects of

irradiation by $^{60}$Co gamma-rays in GaN are charge compensated suggesting that the primary defects generated are N lattice Frenkel pairs.

The energy threshold for atomic displacement is notably higher for Ga than that of N in GaN [52]. As revealed by molecular dynamics calculations, the lowest displacement energies for Ga and N are 39 and 17 eV, respectively. The weighted average displacement energies taking into account wurtzite crystal orientation are 73.2 for Ga and 32.4 eV for N. When irradiated by high energy (0.7 – 1.0 MeV) electrons, Frenkel defects are generated far less in the Ga lattice for electron energies below 400 keV, while for the N lattice the Frenkel pair generation rate is nearly constant after 150 keV [51]. With gamma-rays from $^{60}$Co of energy above 1 MeV, the dominant process, Compton scattering, imparts an average energy of 600 keV to scattered electrons. The generation of Frenkel defects at 600 keV is more than twice as frequent for the N lattice as compared to the Ga lattice. For GaN, the impact of internal electron irradiation was found to be equivalent to $^{60}$Co gamma irradiation [53].

The minority carrier diffusion length in GaN has been established to be dependent upon carrier concentration and defect density. In p-type GaN it was demonstrated that the value of L was on average 500 nm longer for MOCVD than for MBE produced GaN [12].

### *3.1.2 Cathodoluminescence Emission*

#### 3.1.2.1 Continuous wave cathodoluminescence

Samples of GaN were produced via MOCVD and HVPE and were used for comparison. The emission spectrum produced by MOCVD-GaN, presented in Figure 7, shows a strong peak emission centered at 365 nm.

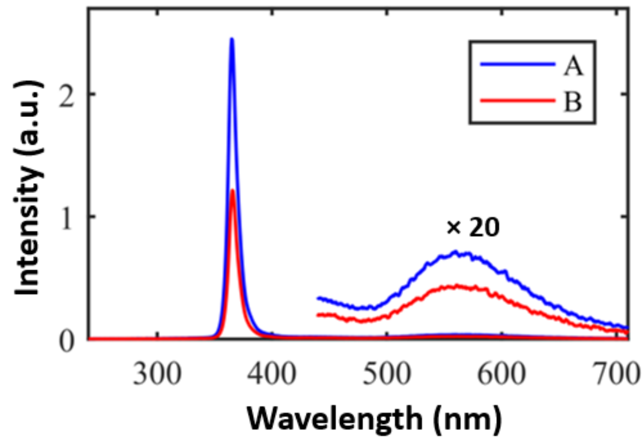


Figure 7. CL spectra of MOCVD-produced GaN.The two spectra presented represent the high (A) and low (B) bound for spectral emission over a 2.5 µm × 2.5 µm area. The spectra beyond 450 nm is multiplied by 20 to enhance for comparison.

A simple relation can be used to easily convert between wavelength and energy, namely

$$hc \simeq 1240\ nm \cdot eV \tag{16}$$

where h is Planck's constant and c is the speed of light. Using equation (16) and observing the CL emission in Figure 7, the peak emission at 365 nm corresponds to an energy of ~ 3.397 eV, the bandgap energy of GaN. Also evident in the GaN spectra is a weaker and broader peak centered at ~ 570 nm (2.175 eV). This peak represents alternate recombination pathways which are less energetically favorable than the band to band recombination, but only slightly so. This peak, known as a *defect band*, arises due to the population of defects in the material, the broadness is indicative of the electronic states at the defects being similar. For the MOCVD sample the defect band is approximately 1/60 of the intensity of the peak at the bandgap.

Spectral CL mapping was performed on the MOCVD-produced samples using the Attolight instrument. The coincident collection of SEM and CL images is presented in Figure 8.

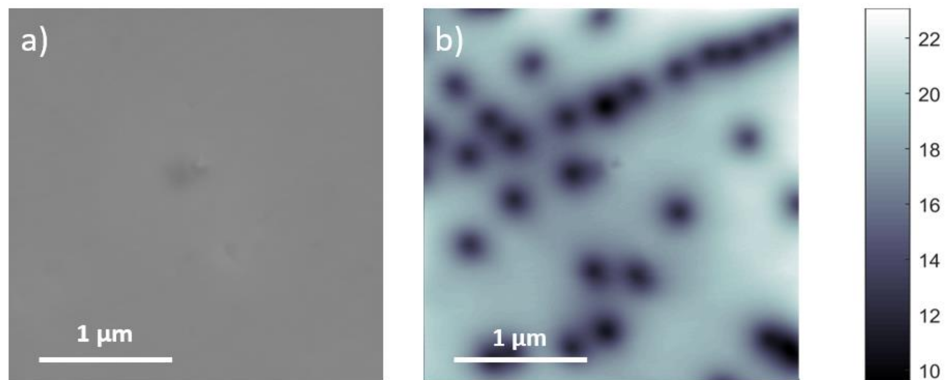


Figure 8. SEM and CL images of GaN produced by MOCVD. Images collected of the same area collected simultaneously on Attolight instrument with a 6kV accelerating voltage and a pixel depth of 512 × 512. The CL image is at 365 nm with a 5 nm FWHM bandwidth.

Comparison of the images reveals a spatial variation in CL intensity, while a blemish at the center of each confirms their coincidence. The darker regions in the CL image correspond to threading dislocations in the GaN lattice. The influence of the average threading dislocation reaches a span of approximately 220 ± 25 nm at a surface density of 7.4 x $10^8$ $cm^{-2}$. By using the density of GaN, 6.15 g/$cm^3$, in equation (6), $R_e$ in GaN at a beam energy of 6 keV is approximately 150 nm. A comparison of the MOCVD and hydride vapor phase epitaxially (HVPE)-grown GaN (see Figure 9) shows a stark contrast in the density of threading dislocations by method.

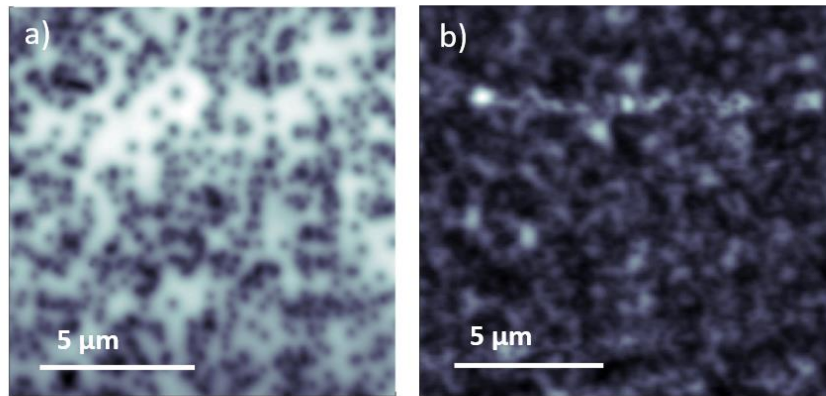


Figure 9. Comparison of continuous CL for (a) MOCVD and (b) HVPE-produced GaN. Each image was collected at 6 kV with a 512 × 512-pixel depth on the Attolight instrument.

Noting the heavy dislocation density in the HVPE produced sample, experimentation proceeded with the MOCVD produced GaN.

3.1.2.2 Pulsed mode cathodoluminescence

The pulsed beam excitation (as described in § 2.5.1.2 Pulsed mode excitation) was applied to the MOCVD produced GaN. For room temperature, the resulting streak is presented in Figure 6. Streak data was collected for GaN at 6 kV for various points in the scene of Figure 8 (b) and the wavelength-integrated spectra are presented in Figure 10.

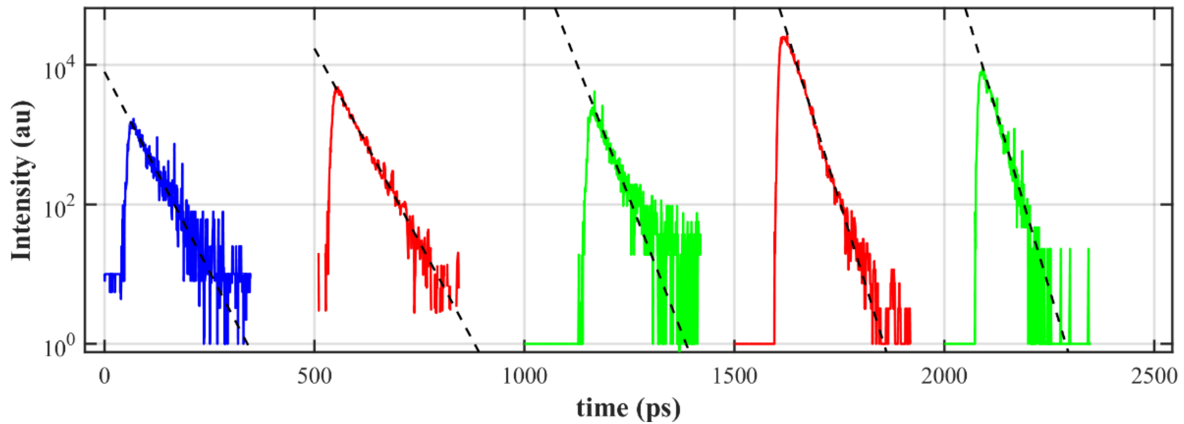


Figure 10. Fitting applied to streak data from GaN at room temperature. Time constants extracted from various points from MOCVD-produced GaN. From equation (1) and assuming N = 1, the values from left to right of $\tau_1$ are 37.9, 39.1, 28.1, 22.4, and 21.6 ps.

The variety of temporal behavior available represents a spatial variation in the recombinative properties of the sample, which is easily attributable to the presence of the threading dislocations. The density of threading dislocations can vary depending on production method, Threading dislocations have been shown to reduce decay lifetime and luminescence. This has been attributed to the charge concentration gradient induced near the dislocation, which behaves as a junction and allows for non-radiative recombination pathways [54].

The effects of temperature on the recombinative behavior of the threading dislocation were investigated. Presented in Figure 11 is the fastest decays found in a scene at a given temperature.

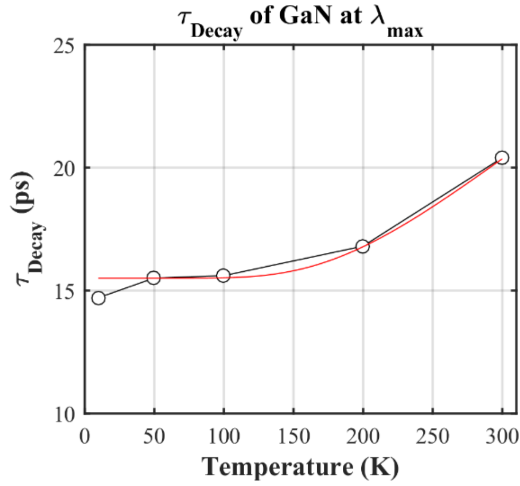


Figure 11. Fastest decays found for GaN as a function of temperature. These time constants of decay for GaN as a function of temperature represent the smallest values achieved at each temperature. The red line is a fit described by equation (17) and assuming $E_a$ = 90 meV, A = 47.5 µs, and $\tau_0$ = 15.5 ps.

The fit line in Figure 11 was derived semi-phenomenologically by substituting equation (3) and the right-side equality of (13) to find

$$\tau \propto A \exp\left(-\frac{E_a}{k_B T}\right) + \tau_0 \tag{17}$$

where A is a constant, $E_a$ is the thermal activation energy, $k_B$ the Boltzmann constant, T the temperature, and $\tau_0$ a constant. The value of $E_a$ was found to be approximately 90 meV. The constant $\tau_0$ can be thought of as constant above 50 K though there was a small deviation from the minimum decay found at 10 K which was 14.7 ps. This could indicate another temperature dependent radiative recombination pathway with a much smaller thermal activation energy.

### 3.1.3 Low-dose $^{60}$Co Impact on AlGaN/GaN-based HEMT Devices[2]

The tested HEMTs were grown on Si wafers via MOCVD with standard precursors in a cold-wall, rotating disc reactor. The process began with an AlN layer in direct contact with the Si wafer in order to avoid Ga-Si interactions. The device heterostructure consists of an AlGaN transition layer, ~800 nm GaN buffer layer and a 16nm $Al_{0.26}Ga_{0.74}N$ barrier layer. GaN and AlGaN layers were grown at 1030 °C. Transistor fabrication began with Ti/Al/Ni/Au Ohmic contact metallization with Ni/Au and rapid thermal annealing in flowing $N_2$ at 825 °C for 30 s. Inter-device isolation was accomplished with the implantation of multiple energy $N^+$ in order to produce significant lattice disruption throughout the GaN buffer layer. Ion implantation helps to maintain planar geometry through the device, helping to reduce parasitic leakage paths that may exist in passivated and isolated HEMTs. Directly following ion implantation, the devices were passivated with ~70 nm of $SiN_x$ using plasma enhanced chemical vapor deposition (PECVD), with a sample temperature of 300 °C [39]. Patterning of the Schottky gate and windows to the Ohmic contact pads was then performed by selective removal of the passivation layer. With gate and Ohmic contact pads open, metallization of both areas occur simultaneously using Ni/Au, followed by another similar passivation layer of $SiN_x$. Contact windows are then opened by dry etching with

---

[2] Portions of § 3.1.3 Low-dose 60Co Impact on AlGaN/GaN-based HEMT Devices are published in Radiation Effects and Defects in Solids, Jonathan Lee, Anupama Yadav, Michael Antia, Valentina Zaffino, Elena Flitsiyan, L. Chernyak, Joseph Salzman, Boris Meyler, Shihyun Ahn, Fan Ren and Stephen J. Pearton. *Low Dose $^{60}$Co Gamma-Irradiation Effects on Electronic Carrier Transport and DC Characteristics of AlGaN/GaN High-Electron-Mobility Transistors,* **172**, Published 19 February 2017.

$SF_6$/Ar and an additional metal deposition of Ti/Au for the HEMT with the source field plate. The field plate is electrically connected to the source terminal and extends by 1 micron over the gate to the gate-drain region. The distances from source to gate and channel length of the devices with and without the source field plate are 1 and 4.7 µm, respectively, with a channel width of 50 µm. Figure 12 (a) shows the SEM image of the device layout.

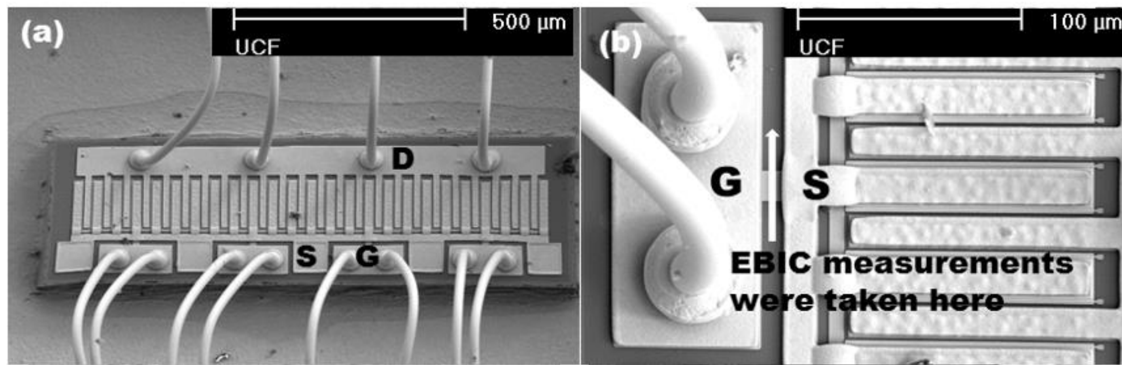


Figure 12. SEM image of AlGaN/GaN HEMT device used for low dose $^{60}Co$ gamma radiation effects. The SEM top view (a) of the AlGaN/GaN HEMTs device layout and (b) showing the area where EBIC measurements were taken [55].

In order to explore the effect of gamma radiation on minority carrier transport properties, EBIC measurements were performed on AlGaN/GaN HEMTs. Measurements were first taken prior to gamma irradiation and were repeated with devices exposed to increased doses of radiation. Devices were exposed to $^{60}Co$ gamma radiation to accumulate doses of 100, 200, 300, 400 and 600 Gy. The irradiation was performed by NORDION, Inc at room temperature in an inert nitrogen environment at a rate of ~2 Gy/s. Source, gate and drain electrodes were kept electrically grounded during irradiation. This prevents the influence of high electric field stress and self-heating of the devices.

Measurements were taken between the source and gate terminals *in situ* using the Phillips XL30 Scanning Electron Microscope with a 20 kV accelerating voltage. EBIC data were extracted by scanning the SEM's electron beam perpendicularly from the edge of the gate contact and recording the exponential decay of the current measured at the source contact. Figure 12 (b) shows the profile of EBIC line-scan taken on HEMT devices. Each measurement was taken at various locations to avoid areas on the sample that may be potentially impacted by the previous exposure to electron beam. For each dose of gamma irradiation, temperature-dependent minority carrier diffusion length measurements were carried out by increasing the temperature incrementally from 25 to 125 °C using a hot stage and an external Gatan temperature controller. The $E_a$ extracted from these measurements bears the information of the defect levels involved in the recombination process for the charge carriers.

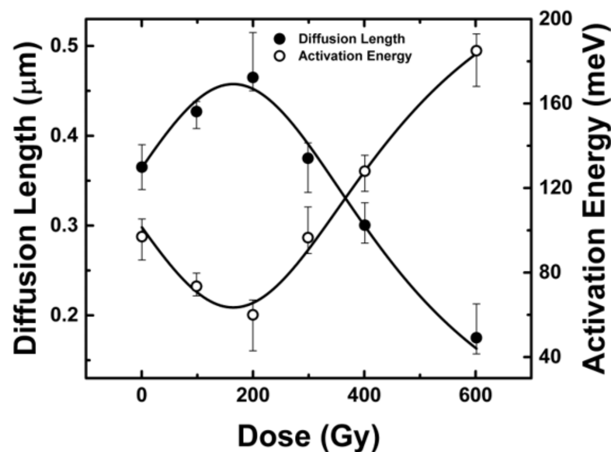


Figure 13. Experimental dependence of minority carrier diffusion length (left axis, closed circles) and activation energy (right axis, open circles) on irradiation dose [55].

Figure 13 shows that for low doses of gamma-irradiation (≤ ~250 Gy), diffusion length increases about 40% with an increased dose of gamma-irradiation while the associated activation

energy exhibits a decrease, the error bars represent the error in the measurement of a single device tested five times for each dose.

### *3.1.4 General Discussion*

The results of CL confirm a direct bandgap of ~ 3.4 eV and a recombination lifetime between 20 and 40 ps. The electron beam-excited carrier radiative recombination lifetime showed a spatial variation with dependence on the influence of threading dislocations which have reduced CL intensity. The temperature dependence of the carrier recombination lifetime in vicinity of threading dislocations revealed an activation energy of approximately 90 meV and is attributed to the nitrogen vacancies in the material.

The variation of L and $E_a$ is due to the creation of defects in III-N layers, generated by the interaction of $^{60}$Co gamma-photons with the material. These defects introduce additional energy states (meta-stable levels) in the bandgap [50, 56], and can act as supplementary recombination centers. The increase in the diffusion length observed after low dose gamma-irradiation is a consequence of a decrease in the number of recombination events for non-equilibrium carriers. Compton electrons, caused by gamma-irradiation, generate additional non-equilibrium electron-hole pairs. During the latter process, a non-equilibrium electron falls into a meta-stable trap (a defect level within the band gap). This will prevent the future capture of another non-equilibrium carrier on the trap, because it is already occupied, and therefore will reduce the number of recombination pathways [50, 57], thus increasing the minority carrier lifetime.

The improvement of transport properties in AlGaN/GaN HEMTs after being exposed to low doses of gamma-irradiation has been demonstrated. It was shown that low (below ~250 Gy)

and high doses (above ~300 Gy) of gamma-irradiation effect the AlGaN/GaN HEMTs differently. The devices displayed a considerable ~26 % improvement in L after exposure to low doses of gamma-irradiation. This is likely associated with an irradiation-induced growing lifetime of the non-equilibrium carriers. For doses above 300 Gy, the impact of defect scattering is more pronounced, leading to the degradation of carrier mobility, and decrease of L.

## 3.2 Minority Carrier Transport Properties in β-$Ga_2O_3$

### *3.2.1 Prior State of the Art*

The optical properties of β-$Ga_2O_3$ have been investigated to find a heavy influence on dopant species and concentration [58, 59]. Dopants with charge greater than three (including Si) led to an emission near the UV/Visible light border at ~ 380-400 nm, while doping with beryllium (Be) alone or lithium (Li) plus another triply chargeable ion will induce a green emission near 500 nm [59]. The Fermi-Dirac statistical distribution described in equation (12) is obeyed in Harwig and Kellendonk's temperature dependence of CL intensity at green (~ 500 nm) and blue (~ 420 nm) wavelengths, however, their analysis did not include determination of the parameters [58].

The bandgap energy is commonly described as direct and estimated to be 4.9 eV, as spectral photoresponse and transmission/absorption measurements place the cutoff wavelength at about 250 nm in each case [59, 60]. The emission characteristics of β-$Ga_2O_3$ are similar to that of an indirect bandgap semiconductor. The common emission bands have been estimated to be representable by a few discreet Gaussian energy bands and lie well below the bandgap energy. The band at 3.65 eV is consistent with the charge transition level for one of the three inequivalent

oxygen vacancy ($V_O$) sites [61]. The emission at 3.25 eV is attributed to the recombination of free electrons with self-trapped holes [62] while that of 2.9 eV is attributed to donor-acceptor pairs [60].

The temporal characteristic of excited carrier decay either by PL [63] and CL [59] is that of a fluro-phosphor displaying a fast and slow luminescence component. This is consistent with equation (1) for N = 3. In the study by Binet and Gourier [64], the TRPL decay from the UV (3.2 eV) luminescence was not observed at t < 100 ns. The thermoluminescence behavior was observed by Vastil'tsiv *et. al* showed a strong peak emission at 140 K followed by a much weaker and broader peak at 385 K, each centered at 520 nm [65].

### *3.2.2 Cathodoluminescence Emission*

The samples in this study consisted of epitaxially grown β-$Ga_2O_3$ on single crystal Sn-doped β-$Ga_2O_3$ substrates. The Sn-doped substrates were grown by Tamura Corporation (Japan) via edge-defined film-fed method and showed (001) surface orientation. The carrier concentration in the substrates was determined by collaborators from Hall measurements to be $3.6\times10^{18}$ $cm^{-3}$ [66]. HVPE was used to grow epitaxial layers which contained ~ 1% Si-doping by Novel Crystal Technology. Epitaxial layers were ~ 20 µm thick initially, and subsequently subjected to chemical mechanical polishing, reducing the final thickness to ~ 10 µm [67].

#### 3.2.2.1 Continuous wave cathodoluminescence

The continuous wave CL emission was recorded using the Attolight instrument and the data is presented below. The primary emission peak was found at ~ 380 nm (3.26 eV) with about

an 80 nm FWHM bandwidth. The CL spectrum is presented in Figure 14 along with a sum of Gaussian fit curves according to

$$I_{CL}(\lambda) = \sum_{i=1}^{N} a_i \exp\left(-\left(\frac{\epsilon(\lambda) - b_i}{c_i}\right)^2\right) \tag{18}$$

where $a_i$, $b_i$, and $c_i$ are constants associated with the Gaussian fitting conditions in Figure 14, the values of the constants used is listed in

Table 2. This fitting method is very general for spectra and must be used with caution since nearly any spectrum can be represented by the sum of a series of Gaussian curves. However, the fit error was very low using N = 3 as ascribed in ref. [60] for samples with Si doping.

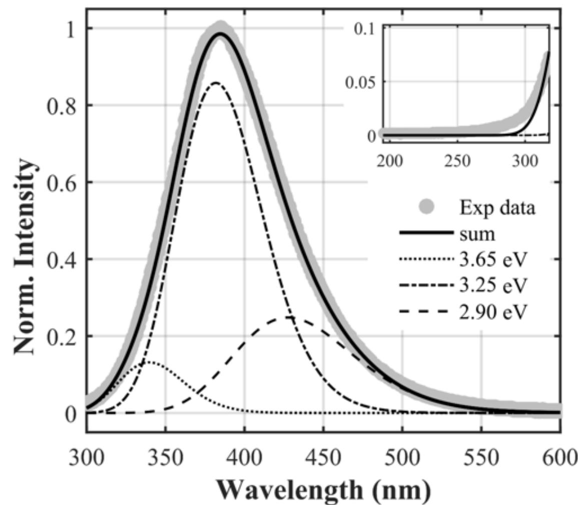


Figure 14. Continuous wave CL of β-$Ga_2O_3$ collected at room temperature and 6 kV accelerating voltage presented with Gaussian breakdown. The main window presents the normalized intensity spectrum (gray circles) from 300 to 600 nm with the estimated Gaussian peaks centered at 3.65 (dotted), 3.25 (dot-dashed), 2.90 eV (dashed), and the sum of the Gaussian peaks (solid). The inset presents the spectrum from 200 to 320 nm showing absence of bandgap emission [68].

Table 2. Parameters for Gaussian deconvolution of continuous wave CL emission of β-$Ga_2O_3$. The constants for evaluation of Gaussian peaks defined in equation (18) and present in Figure 14.

| Band Energy | $a_i$ (a.u.) | $b_i$ (eV) | $c_i$ (eV) | $FWHM_i$ (eV) |
|---|---|---|---|---|
| $E_1$ = 3.65 eV | 0.13 | 3.65 | 0.31 | 0.52 |
| $E_2$ = 3.25 eV | 0.86 | 3.25 | 0.33 | 0.55 |
| $E_3$ = 2.90 eV | 0.25 | 2.90 | 0.36 | 0.60 |

As noted in Figure 14, and consistent with previous studies, an emission from the bandgap energy was absent. The CL signal intensity with respect to voltage was also demonstrated to show the intensity dependence on accelerating voltage and is presented in Figure 15. Also shown is the emission spectra out to longer wavelengths showing a defect band at about 680 nm (1.82 eV).

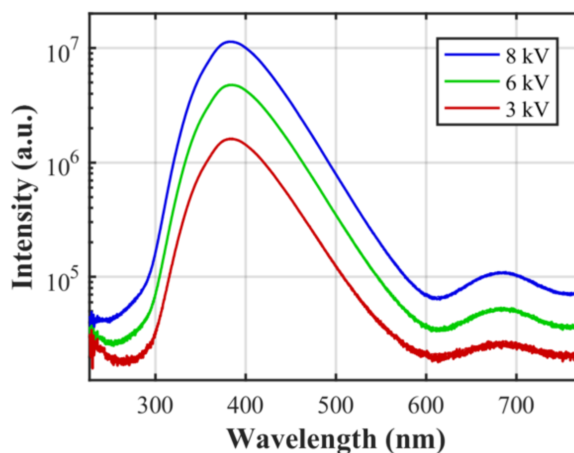


Figure 15. CL emission spectra for Si-doped β-$Ga_2O_3$ by accelerating voltage. The primary luminescence was observed at ~ 380 nm, intensity is set to log-scale to enhance viewing of the defect band at 680 nm.

The defect band is likely due to the prevalence of dislocation type defects from the HVPE film production and the interference in the lattice caused by Si inclusions. The beam currents for the

8 and 6 kV cases were nearly equivalent, while their relative emissions are not. Thus, the influence of accelerating voltage on CL emission intensity is quite significant, this is attributed to the size of the generation volume leading which may enclose more carriers which can recombine radiatively. One can equivalently describe the situation as electrons with more energy will scatter more times and excite more carriers in general than lower energy electrons and hence lead to a higher intensity.

CL imaging of the surface of β-$Ga_2O_3$ was accomplished from spectral map collection and integrated from 370 to 390 nm. The comparison of SEM and CL images is presented in Figure 16 for 3, 6, and 8 kV accelerating voltages. The constellation of dark spots in the upper right corner of in the images confirms each image is of the same area.

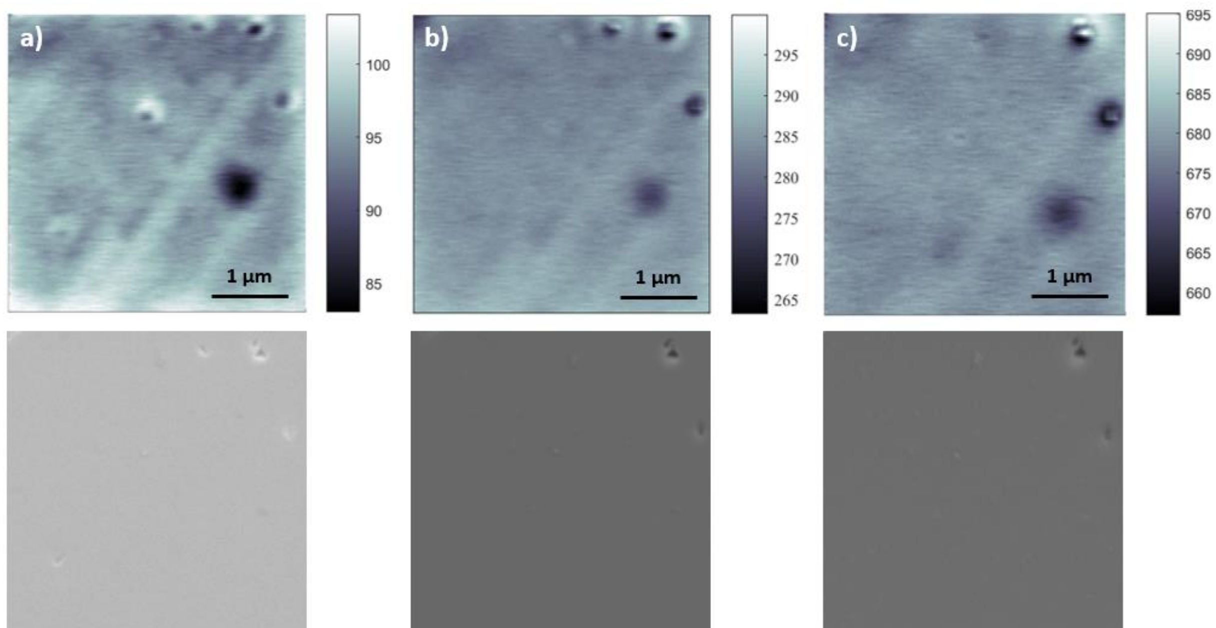


Figure 16. CL (top) and SEM (bottom) micrographs of β-$Ga_2O_3$. Images presented for (a) 3, (b) 6, and (c) 8 kV, CL images were integrated with a 20 nm bandwidth around 380 nm. The scalebars apply to both CL and SEM images.

The dark spots are likely from the mechanical defects in the surface, since they are visible in their SEM counterparts. The large darkened area in the middle right was the spot used for CL focusing and anecdotally demonstrates first evidence of electron injection impact on β-$Ga_2O_3$, which will be a topic of discussion in a later section. There are yet other distinct surface characteristics especially visible in the 3 kV image in Figure 16 (a) due to the reduced $R_e$ of ~ 47 nm. The streak-like features are likely related to edge dislocations in the surface layers. Their influence on the CL image is diminished upon increasing accelerating voltage due to the enlargement of the generation volume and the electron range in the material.

#### 3.2.2.2 Pulsed mode cathodoluminescence

The broadness of the spectral luminescence from β-$Ga_2O_3$ was quite disperse as compared to GaN, which made for a lower signal-to-noise ratio at the streak camera output. To accommodate this, the beam was operated at 10 kV accelerating voltage and the collection was run 4 times

longer than that of GaN. Further, the UV/blue emission found at 3.25 eV has been found to have fluorescent and phosphorescent emissions, meaning there is a persistent luminescence on the

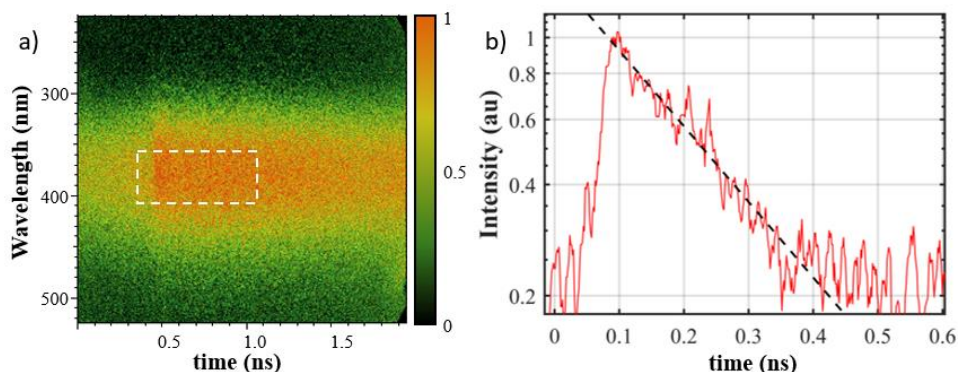


Figure 17. Streak data for β-$Ga_2O_3$ at room temperature and 10 kV accelerating voltage. Streak data (a) with dashed box indicating the data integration region to generate the normalized decay curve (b) with fit line from equation (1) using N = 1 and τ = 205 ps [68].

timescale of $10^{-7}$ s [59] to $10^{-5}$ s [64] depending on dopant and experimental conditions.

Due to the 80 MHz (period of 12.5 ns) cycle rate of the streak camera, should the luminescence exceed $10^{-7}$ s it could be present as a background signal. The background signal observed was nearly flat over the entire accessible range of the detector, indicating the presence of a long decay which cannot be analyzed without special preparations (installation of a frequency halving adjustment to the pulse system). The primary luminescence band at 380 nm was located and found to have a room temperature decay lifetime of approximately 210 ± 20 ps.

### *3.2.3 Effect of Surface Etching on β-$Ga_2O_3$*[3]

There have been a few studies of wet etching of $Ga_2O_3$, where it was found that $HNO_3$ at elevated temperature and hydrofluoric acid at room temperature provide the fastest removal rates [70]. Dry etching is preferable because of its higher resolution, and control and initial studies of reactive ion etching (RIE) and inductively coupled plasma (ICP) etching in predominantly chlorine or boron trichloride ($Cl_2$, $BCl_3$) plasma chemistries have shown removal rates up to ~1500 Å $min^{-1}$ under high power conditions [71]. The presence of electrical damage in the near-surface region of ICP etched $Ga_2O_3$ was found through barrier height changes of Schottky diodes fabricated on the etched surface [71].

Experiments were performed with bulk β-phase (-201) oriented $Ga_2O_3$ single crystals from Tamura Corporation (Japan) grown by the edge-defined film-fed growth method. Hall effect measurements showed that the sample was unintentionally n-type with an electron concentration of ~$3 \times 10^{17}$ $cm^{-3}$. Full-area back Ohmic contacts were created using Ti/Au (20 nm/80 nm) deposited by e-beam evaporation. Linear current–voltage behavior was obtained without the need for a rapid annealing step. Unmasked samples were exposed to 15 $BCl_3$/ 5 Ar discharges (where the numbers represent the respective gas flows in standard cubic centimeters

---

[3] Portions of § 3.2.3 Effect of Surface Etching on β-Ga2O3 are published in Journal of Vacuum Science and Technology B, Jiancheng Yang, Fan Ren, Rohit Khanna, Kristen Bevlin, Dwarakanath Geerpuram, Li-Chun Tung, Jingyu Lin, Hongxing Jiang, Jonathan Lee, Elena Flitsiyan, Leonid Chernyak, S. J. Pearton and Akito Kuramata. *Annealing of dry etch damage in metallized and bare (-201) $Ga_2O_3$,* **35**, Published 25 July 2017..

per minute) in a Plasma-Therm Versaline ICP reactor. The 2 MHz power applied to the three-turn ICP source was 400 W, while the rf (13.56 MHz) chuck power was 200 W. The dc self-bias on the sample electrode was ~450 V. The $Ga_2O_3$ etch rate under these conditions is ~700 Å $min^{-1}$, and the samples were etched for 3 min. Schottky contacts were prepared on the front sides of the samples after etching by e-beam deposition of Ni/Au (20 nm/80 nm) contacts through a stencil mask.

Minority carrier diffusion length measurements were carried out by recording the exponential decay of EBIC as a function of the distance from the gate, see equation (7). The influence of $v_s$ was assumed to be negligible (i.e., $v_s = 0$; $\alpha = -0.5$). Each diffusion length determination was an average of a minimum of seven measurements. All the measurements on the devices were performed *in situ* in the Philips XL-30 SEM under an accelerating voltage of 16 kV, corresponding to an estimated $R_e$ of 870 nm, and current pre-amplifier gain of 2 nA/V. EBIC data were acquired by scanning the electron beam of the SEM along a line perpendicular to the edge of gate contacts and recording the exponential decay of the current. A portion of the data from the reference sample is presented in Figure 18.

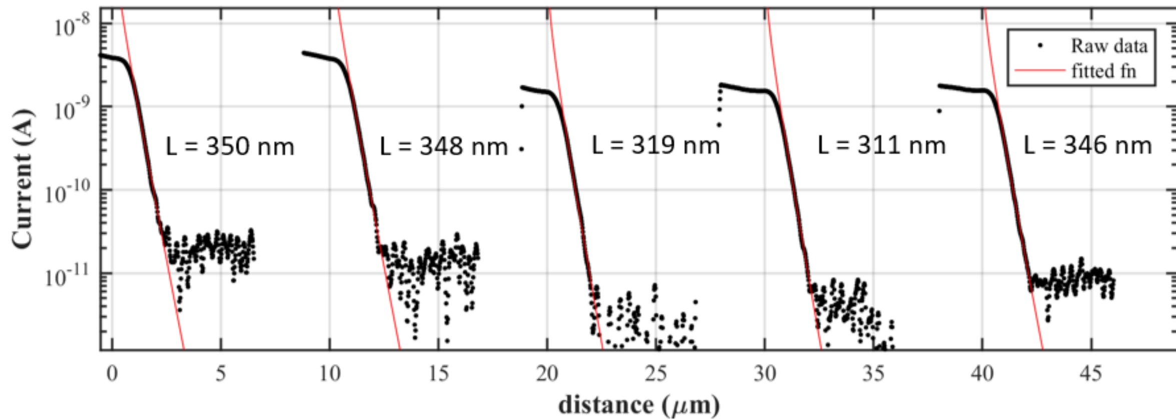


Figure 18. EBIC data for (-201)-oriented β-$Ga_2O_3$ reference sample. Presented along with the corresponding fit, according to equation (7) with α = -0.5, and the values of L.

Since EBIC is a minority carrier sensitive method, this is the minority carrier (hole) diffusion length along the (-201) face. There are noticeable deviations from the mean value, which did not rely on angular placement along the Schottky.

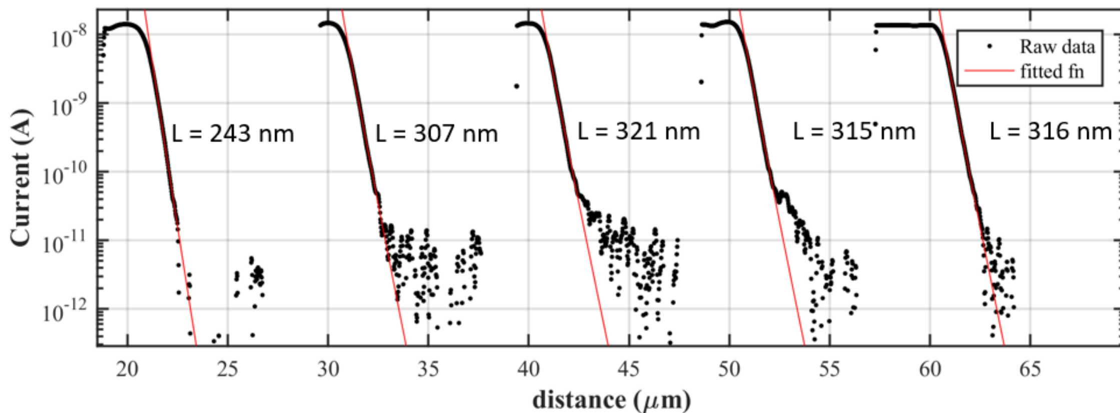


Figure 19. EBIC data for (-201) oriented β-Ga2O3 after 3 minutes of 400 W of ICP etching. Presented along with their corresponding fit according to equation (7) with α = -0.5, and the values of L.

The ICP etch damage of 3 minutes led to a slight reduction in L from 350 ± 75 nm to 305 ± 43 nm. The etched sample EBIC data is presented in Figure 19. Since the surface recombination did not appreciably change and L was reduced, a likely explanation is that point defects are have been

introduced via ICP, another possible explanation is the introduction of surface strain. The damage is created by energetic ion bombardment but in some cases may also consist of changes to near-surface stoichiometry through the preferential loss of one of the lattice elements or deposition of etch residues. This damage was found to be significantly reduced by annealing at 400 °C, however this noticeably reduced the height of the Schottky barriers [69].

### 3.2.4 *Impact of 10 MeV Proton Irradiation*[4]

The carrier removal rates for proton irradiation are found to be comparable to those in GaN of similar doping levels and fluences [73-75]. The main defect created in $Ga_2O_3$ by proton irradiation has been identified as a Ga vacancy with two hydrogens attached [76].

The samples were bulk β-phase $Ga_2O_3$ single crystal wafers (~650 µm thick) with (001) surface orientation grown by the edge-defined film-fed growth method. Hall measurements showed the Sn-doped samples had carrier concentration of $2.2 \times 10^{18}$ $cm^{-3}$. Epitaxial layers (initially ~20 µm thick) of lightly Si-doped (~$3 \times 10^{16}$ $cm^{-3}$) n-type $Ga_2O_3$ were grown on these substrates by HVPE. After growth, the epi-surface was subjected to chemical mechanical polishing to planarize the surface, with a final thickness of ~10 µm. Diodes were fabricated by depositing a full area back Ohmic contacts of Ti/Au (20 nm/80nm) by e-beam evaporation. The

---

[4] Portions of § 3.2.4 Impact of 10 MeV Proton Irradiation are published in Journal of Vacuum Science and Technology B, Jiancheng Yang, Zhiting Chen, Fan Ren, S. J. Pearton, Gwangseok Yang, Jihyun Kim, Jonathan Lee, Elena Flitsiyan, Leonid Chernyak and Akito Kuramata. *10 MeV proton damage in β−$Ga_2O_3$ Schottky rectifiers,* **36**, Published 8 January 2018.

front sides were patterned by lift-off of electron beam deposited Schottky contacts Ni/Au (20 nm/80 nm) with a diameter of 210 µm.

The 10-MeV proton beam was generated using a MC-50 Cyclotron at the Korea Institute of Radiological and Medical Science. The proton beam was injected into a low-vacuum chamber, where the $\beta$-$Ga_2O_3$-based devices were loaded, facing the proton beam. The average beam-current, measured by Faraday-cup, was 100 nA during the proton irradiation process. Proton fluence was fixed at $10^{14}$ $cm^{-2}$. The projected range of the 10-MeV proton beam was calculated using the stopping and range of ions in matter program and is 330 µm, which is well into the substrate. Minority carrier diffusion length, L, was determined as previously using the EBIC method on the aforementioned Schottky contacts. The EBIC was recorded during line-scans of 10 s duration performed *in-situ* in the Philips XL-30 SEM operated at 20 keV ($R_e$ ~ 1.3 µm). The room temperature value of L was ~340 nm for the nonirradiated sample and decreased with increasing temperature due to increased scattering or recombination. After proton irradiation, the room temperature diffusion length was reduced to ~315 nm. The values of the activation energy according to equation (11) were 41.8 and 16.2 meV and the asymptotic $L_0$ values were 145 and 228 nm for the nonirradiated and proton irradiated samples, respectively.

The excited carrier lifetime was observed by TRCL at room temperature using the Attolight instrument and was found to be ~ 215 for the reference and 300 ps for the proton irradiated sample.

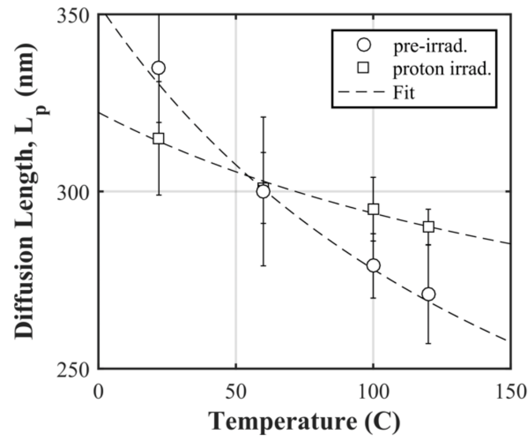


Figure 20. Minority carrier diffusion length in (001) Si-doped β-$Ga_2O_3$ for reference and 10 MeV proton irradiated sample. The activation energies according to equation (11) are 41.8 and 16.2 meV for the reference and irradiated sample, respectively [72].

The indication of the behavior of L with temperature is that the types of defects generated tend to insulate L against temperature-induced reduction at temperatures above 60 °C. It is likely that the implanted hydrogen atoms remain as shallow donors and increase n-type conductivity. Hydrogenic inclusions in $Ga_2O_3$ have been demonstrated to have an activation energy of about 15 meV as determined by muon-spin rotation and relaxation spectroscopy μSR [77].

Table 3. Material parameters for Si-doped β-$Ga_2O_3$ in response to 10 MeV proton irradiation. After ref. [72].

| Fluence | n ($cm^{-3}$) | L (nm) | $L_0$ (nm) | $E_a$ (meV) | τ (ps) |
|---|---|---|---|---|---|
| Non-irradiated | $3.1 \times 10^{16}$ | 340 ± 22 | 145 | 41.8 | 215 ± 22 |
| $1 \times 10^{14}$ $cm^{-2}$ | $8.03 \times 10^{15}$ | 315 ± 16 | 228 | 16.2 | 300 ± 35 |

The result was carrier removal in the epilayer by nonionizing energy loss which created electron traps and acceptor states that compensate the initial donor doping. The calculated carrier removal rate was 235.7 $cm^{-1}$ for the 10 MeV protons. The initial carrier density of 3.1 ×

$10^{16}$ cm$^{-3}$ was reduced to 8.03 × $10^{15}$ cm$^{-3}$ after proton irradiation and annealing at 300 °C restored this approximately half-way, to 1.87 × $10^{16}$ cm$^{-3}$. The carrier removal rates for proton irradiation are found to be comparable to those in GaN of similar doping levels and fluences [73-75]. The main defect created in $Ga_2O_3$ by proton irradiation has been identified as a Ga vacancy with two hydrogens attached [76].

### *3.2.5 Impact of 1.5 MeV Electron Irradiation*[5]

Sample description can be found in § 3.2.4 Impact of 10 MeV Proton Irradiation. The effects of 1.5 MeV electron irradiation on Si-doped β-$Ga_2O_3$ Schottky rectifiers have previously resulted in a carrier removal rate – defined as loss in carrier density (cm$^{-3}$) per fluence (cm$^{-2}$) – of ~ 4.9 cm$^{-1}$ and a significant reduction in reverse-bias current density for higher voltages [67]. Majority electron concentrations in the epitaxial layers are summarized in Table 4.

Irradiation was performed at Korea Atomic Energy Research Institute for fluences of 1.79×$10^{15}$ and 1.43×$10^{16}$ cm$^{-2}$ at a current of 1 mA. L was determined using EBIC technique on Schottky barriers (contacts) in the planar configuration. The EBIC was recorded during line-scans of 10 s duration performed in the Philips XL-30 SEM. Using a beam energy of 20 keV ($R_e$ ~ 1.3

[5] Portions of § 3.2.5 Impact of 1.5 MeV Electron Irradiation are published in Applied Physics Letters, Jonathan Lee, Elena Flitsiyan, Leonid Chernyak, Jiancheng Yang, Fan Ren, Stephen J. Pearton, Boris Meyler and Y. Joseph Salzman. *Effect of 1.5 MeV Electron Irradiation on β-$Ga_2O_3$ Carrier Lifetime and Diffusion Length,* **112**, Published 21 February 2018.

μm), the EBIC was measured for each sample, without bias, as a function of distance from the Schottky contact, x. EBIC was recorded for sample temperatures 295, 330, 370, and 395 K.

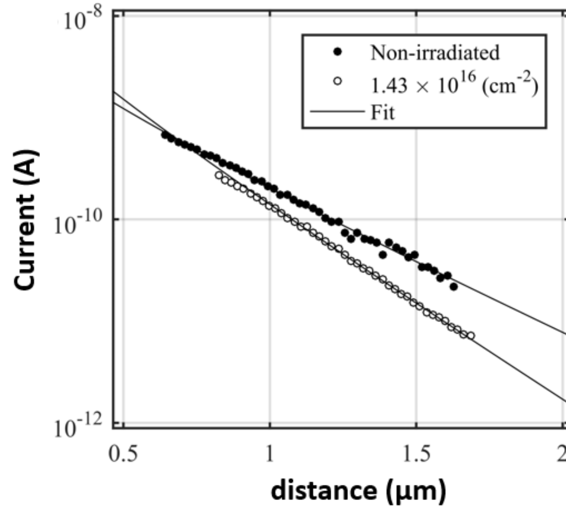


Figure 21. EBIC data for β-$Ga_2O_3$ for reference and 1.5 MeV electron irradiated sample. Presented along with their corresponding fit according to equation (7) with α = -0.5. After ref. [68].

The zero-bias depletion region width in Au/β-$Ga_2O_3$ Schottky diodes has been estimated previously to be d = 14 nm and does not significantly interfere with these measurements since x >> d [78]. To ensure accuracy, the determination of diffusion length is measured at x > 2L [21, 79]. To achieve linearity, the value of α was estimated as -0.5, indicating a low influence of surface recombination velocity. EBIC data are displayed in Figure 21 for the non-irradiated and most irradiated samples along with linear fit generated by equation (7). The values of L are presented in Figure 22 for all temperatures and doses tested.

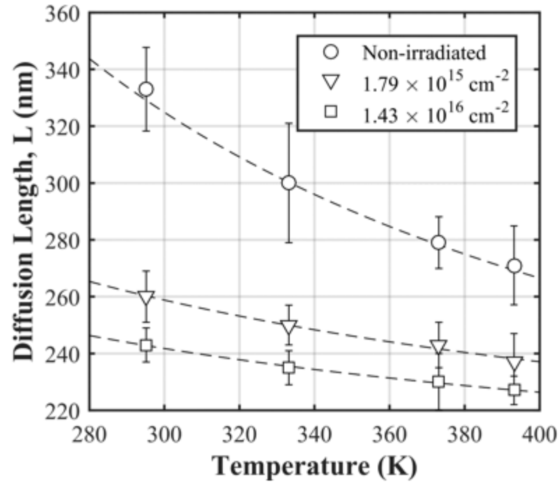


Figure 22. EBIC results of L for β-$Ga_2O_3$ for reference and 1.5 MeV electron irradiated samples. Presented along with their corresponding fit according to equation (11). After ref. [68].

The room temperature value of L was initially 335 nm for the non-irradiated sample and tended to decrease for increasing temperature for all samples. The reduction of L with temperature can be caused by increased scattering or recombination; temperature dependent measurement of lifetime could assist in discerning which dominates. However, present hardware limitations prevent measuring lifetime for higher temperatures and will be addressed in future studies. The values of $E_a$, listed in Table 4, were 40.9 meV for the non-irradiated sample and reduced to 18.1 and ultimately 13.6 meV in response to higher irradiation doses. The introduction of these trap states results in a reduction in L likely due to an increased recombination rate.

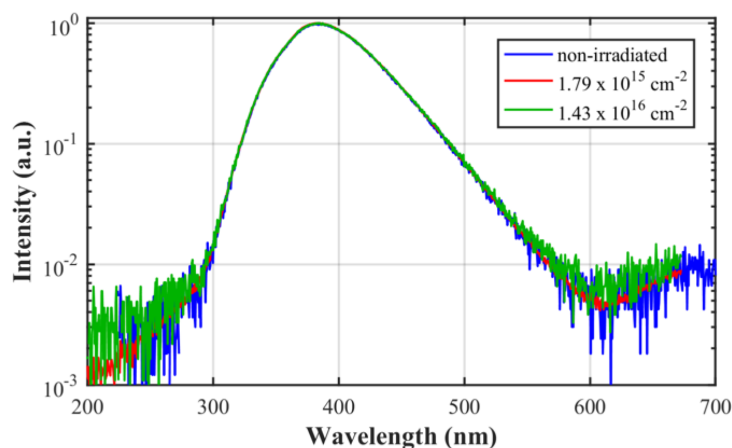


Figure 23. Spectral comparison of continuous wave CL for reference and 1.5 MeV electron irradiated β-$Ga_2O_3$. Each normalized spectrum was collected on the Attolight instrument at 10 kV accelerating voltage.

CL measurements were conducted at room temperature in an Attolight Allalin 4027 Chronos SEM. The accelerating voltage used for all CL measurements was 10 keV. The continuous wave CL spectra for each electron dose is presented in Figure 23. There was no indication of effect on the CL spectra as influenced by electron irradiation. The TRCL technique was utilized to directly measure the decay lifetime, and extracted lifetimes are presented in Figure 24. The values of τ were 215 ps for the non-irradiated sample and reduced to 151 and 138 ps indicating an increase in recombination rate in response to irradiation.

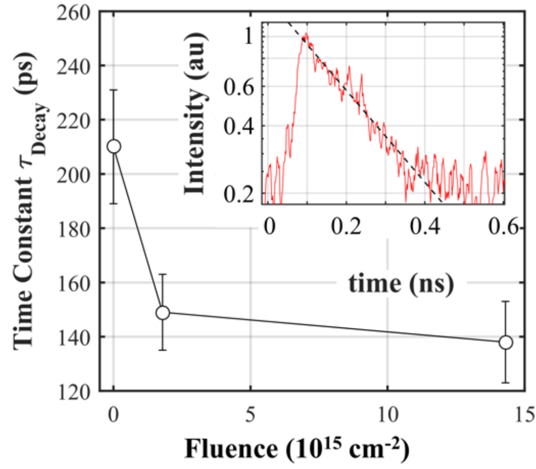


Figure 24. Decay time constant for $\beta$-$Ga_2O_3$ as a function of 1.5 MeV electron fluence. The inset shows a typical decay integrated 20 nm centered at 380 nm and its corresponding fit. After ref. [68].

Table 4. Material parameters for Si-doped $\beta$-$Ga_2O_3$ in response to 1.5 MeV electron irradiation. After ref. [68].

| Fluence | n (cm$^{-3}$) | L (nm) | $L_0$ (nm) | $E_a$ (meV) | τ (ps) |
|---|---|---|---|---|---|
| Non-irradiated | $1.52 \times 10^{17}$ | 333 ± 15 | 147 ± 17 | 40.9 ± 6.8 | 210 ± 20 |
| $1.79 \times 10^{15}$ cm$^{-2}$ | $5.98 \times 10^{16}$ | 260 ± 9 | 182 ± 19 | 18.1 ± 6.2 | 149 ± 14 |
| $1.43 \times 10^{16}$ cm$^{-2}$ | $3.32 \times 10^{16}$ | 243 ± 6 | 186 ± 19 | 13.6 ± 2.4 | 138 ± 15 |

The activation energy of 40.9 meV, found prior to irradiation, matches closely with the donor ionization energy found in previous studies [64, 80-82]. These shallow donor levels have been attributed to Si doping [83]. The irradiation-induced reduction in L and $E_a$ is due to the generation of trap states between the conduction band and the shallow donor levels. The monotonic reduction in activation energy is due to the introduction of these shallow interband traps serving as more energetically favorable pathways for trapped electrons to return to the conduction band and consequently recombine with holes [64]. This is confirmed by the simultaneous reduction in lifetime. The trap states formed are likely due to oxygen displacement,

which can result in either oxygen vacancies, pairs of oxygen and gallium vacancies, or complexes of both. After irradiation, the recombination pathway remains energetically unchanged as evidenced by comparison of continuous wave CL measurements, see Figure 23. While deeper levels may be formed, experimentally we did not observe them. Post-irradiation annealing may repair irradiation-induced defects [84] and move the activation energy toward its pre-irradiated value [85], though it was not performed in this study.

The temperature dependence of minority carrier diffusion length was observed by EBIC and allowed for the extraction of activation energy before and after 1.5 MeV electron irradiation. Exposure to 1.5 MeV electrons led to a marked decrease in L and lifetime suggesting the generation of defects interfering with minority carrier transport. The carrier lifetime was measured by TRCL to determine the effects of irradiation on the ultrafast recombination rate. The initial activation energy was attributed to shallow donor levels commonly found in $\beta$-$Ga_2O_3$ samples, while the irradiated samples displayed reduced activation energy from irradiation-induced trap states. The induced trap states assisted recombination, as evidenced by the reduction in lifetime.

### 3.2.6 Effects of Electron Injection[6]

The effects of electron injection, which were found to be significant in GaN [86] and InGaP [87], were investigated to determine if there is an effect in β-$Ga_2O_3$. The influence of electron injection by electron beam was demonstrated to reduce the continuous wave CL intensity (see Figure 16).

Thick film (several microns) of β-$Ga_2O_3$ was deposited by MOCVD on a c-plane $Al_2O_3$ substrate. Film growth was conducted at 650 °C and 50 Torr using Nitrogen as carrier gas and trimethylgallium ($Ga(CH_3)_3$) as precursor material. The crystallinity and quality of deposited films were assessed using standard methods of XRD, in 2θ mode using Cu $K_\alpha$ radiation source, and micro-Raman spectroscopy, in backscattering geometry using 514.5 nm Ar-ion laser with ~1 µm diameter beam spot size. In order to increase the conductivity of β-$Ga_2O_3$ films, silicon ions were implanted at a particle flux of $1 \times 10^{15}$ $cm^{-2}$ followed by rapid thermal annealing (RTA) in order to activate the implanted silicon atoms. Post-implantation annealing was completed in an Ar environment for 30 s at 900 °C, leaving the surface with a silicon ion density of 1 to $3 \times 10^{17} cm^{-3}$ [88].

Variable temperature (-100 to 100 °C) CL measurements were collected *in situ* in the Philips XL-30 SEM using the Gatan Mono CL2 monochromator. Due to the weak intensity of the

---

[6] Portions of § 3.2.6 Effects of Electron Injection are published in Electrochemical Society Journal of Solid State Science and Technology, Jonathan Lee, Elena Flitsiyan, Leonid Chernyak, Shihyun Ahn, Fan Ren, Lin Yuna, Stephen J. Pearton, Jihyun Kim, Boris Meyler and Joseph Salzman. *Optical Signature of the Electron Injection in $Ga_2O_3$,* **6**, Published October 26, 2016.

near-band-edge (NBE) CL, the accelerating voltage was increased to 30 kV which corresponds to an Re of ~2.6 µm. The CL spectrum at low voltage was observed in order to rule out influences from substrate material. Using an electron beam accelerating voltage of 30 kV, the NBE and visible-range luminescence were observed as a function of electron beam irradiation duration up to 2000 s. For each measurement temperature, the luminescence spectra were taken in a region that was previously unexposed to electron beam irradiation. For each region and temperature, several spectra were taken with an interval of 480 seconds (the approximate time required to collect one spectrum from 200 to 500 nm at 1 nm intervals and 0.1 s integration time).

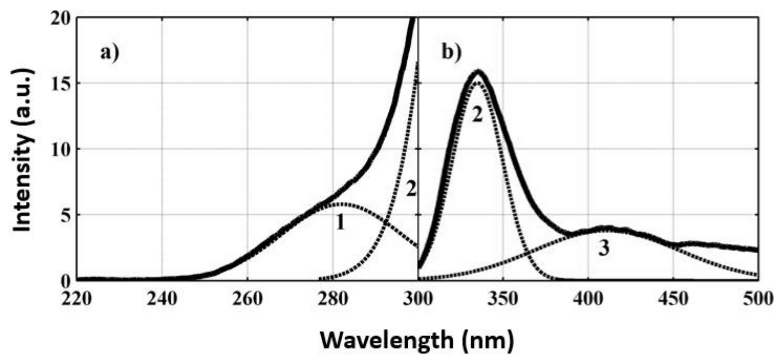


Figure 25. Continuous wave CL of MOCVD grown β-$Ga_2O_3$ on c-plane $Al_2O_3$. The spectrum is divided into two portions, 220 to 300 (a) and 300 to 500 (b) to allow for viewing of the NBE peak, marked 1. The Gaussian fit peaks serve only as a guide to the eyes [82]. Data collected using the Philips XL-30 SEM using 30 kV accelerating voltage.

The primary luminescence peak in this case was ~320 nm, Figure 25 marked as peak 2.

With an intrinsic bandgap energy of ~4.9 eV (~253 nm), the effects of electron injection through CL measurements in the range of 200 - 500 nm were observed. The observed spectra, presented in Figure 25, were collected separately for two distinct regions, from 220 to 300 nm (Figure 25(a)), where a shallow luminescence peak was observed at ~ 285 nm, and from 300 to 500 nm where dominant luminescent peaks were centered at ~ 335 nm and at ~ 410 nm (Figure

25(b)). These spectra were deconvolved and are represented by Gaussian functions displayed in Figure 25, alongside the collected data, which serve to guide the eyes. It is possible that the CL peak at ~ 335 nm is related to Hydrogen point defects present in the material due to the MOCVD growth [77, 89]. The intensity peak centered at 410 nm is likely related to the the implantation of silicon atoms, for comparison see Figure 14. The inclusion of silicon impurities have been found to both induce gallium vacancies and form donor levels below the conduction band [64]. Oxygen vacancies have also been described as electronic donors. While gallium vacancies, combined with nearby oxygen vacancies, can form gallium-oxygen vacancy pairs which form acceptors [65].

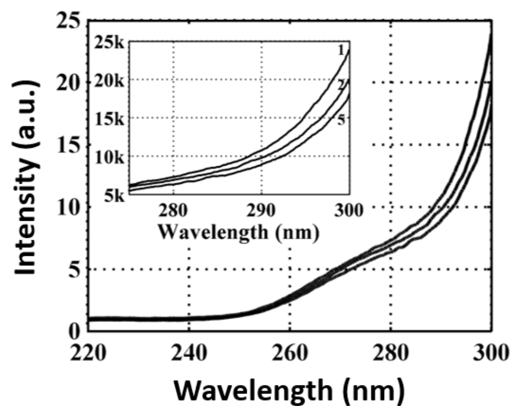


Figure 26. CL spectra collected for MOCVD grown Si-implanted β-$Ga_2O_3$ on c-plane $Al_2O_3$. Collected from 220 to 300 nm and 275 to 300 nm (inset), at 100 °C for SEM irradiation duration of (1) 0 s, (2) 480 s, and (5) 1920 s [82]. Data collected using the Philips XL-30 SEM using 30 kV accelerating voltage.

In order to probe the band-to-band transition the subsequent analysis was focused on the short wavelength region of 280 – 300 nm. Initially, the CL spectrum was collected at -100 °C and was repeated at temperatures of 0, 20 and 100 °C. A distinct decay in CL intensity observed in one of the regions under electron irradiation is presented in Figure 26 for temperature of 100

°C. Similar CL decays were also observed in other regions of the $Ga_2O_3$ sample measured at different temperatures.

The mechanism for CL decay under continuous electron beam irradiation was previously studied in refs. [14, 35, 86], for p-type GaN doped with various impurities (Mn, Fe). Similar to the mechanism proposed in ref. [14], it is suggested that in $Ga_2O_3$, ionized Si-donor levels offer an alternate route for recombination of non-equilibrium electron-hole carriers generated by the SEM beam. While the intensity of CL is proportional to the number of recombination events through donor levels, some of these levels may be excluded from radiative recombination process due to trapping of some portion of non-equilibrium electrons. This trapping may be due to lattice vibrations which increase carrier scattering, making donor levels less available, the non-equilibrium electrons in the conduction band will be "forced" to wait for an available donor level for the radiative recombination, thus increasing their lifetime, $\tau$, in the conduction band. As a result, the number of recombination events will drop with increasing duration of electron beam irradiation and the CL intensity will decrease as seen in Figure 26. As noted in refs. [14, 86] and outlined in § 2.5.3 Thermal Activation Energy of Luminescence, the lifetime of non-equilibrium carriers in the band is proportional to the inverse of CL intensity.

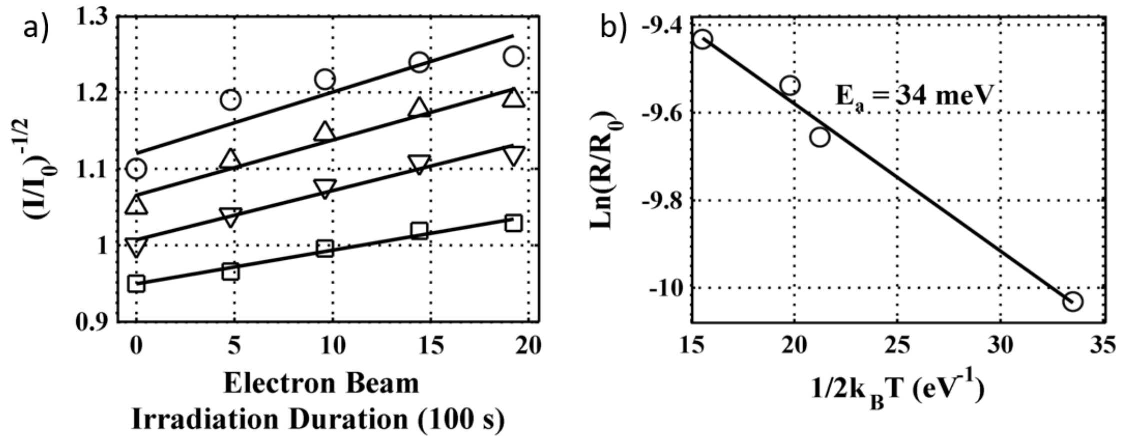


Figure 27. Rate measurements of CL intensity decay for MOCVD grown Si-implanted β-$Ga_2O_3$ on c-plane $Al_2O_3$. The inverse of normalized CL intensity at 298 nm for -100 (squares), 0 (downward triangles), 20 (upward triangles), and 100 °C (circles) and their respective linear fit, vertically offset for clarity. Arrhenius plot of the rate of decay of the inverse of normalized CL intensity experimental data and linear fit [82].

For each temperature tested, the inverse square root of normalized intensity is presented in Figure 27(a) as a function of electron beam irradiation duration. Note that I versus irradiation duration shows a good linear fit, as for GaN. The temperature dependent rate for intensity decrease was obtained from the slope of each experimental dependence in Figure 27(a) and presented in an Arrhenius plot in Figure 27(b). The rate, R, of CL intensity decay is described by equation (14). From the slope of the linear fit in Figure 27(b), $E_a$ is estimated to be approximately 34 meV. This activation energy is possibly related to Si-donor and is comparable to that of its ionization energy [81]. There is also some evidence that oxygen vacancies may be related, since they are also donor defects with an estimated ionization energy of about 36 meV [90]. In p-GaN, the lower rates of intensity decay with increasing temperature indicate the presence of a thermally activated process for trapped non-equilibrium electrons to escape from deep meta-stable Mg-related levels [14]. Present work indicates that in $Ga_2O_3$, there is a competing and

dominating mechanism that is possibly related to interstitial Hydrogen release (from complexes), at elevated temperatures [77, 90, 91].

### *3.2.7 General Discussion*

Minority carrier diffusion lengths for all β-$Ga_2O_3$ samples displayed a decrease in L with temperature. This is contrary to the behavior of some other semiconductor materials, for instance GaN [12] and InAs/GaSb (see below, § 3.3 Minority Carrier Transport Properties in InAs/GaSb Type II Strain-Layer Superlattice), but consistent with Si and GaP [21]. The minority (hole) diffusion length was generally on the order of 250 - 350 nm with carrier lifetime measured by TRCL on the order of 200 ps.

Bulk samples from edge-defined film-fed growth method had a wider variance in the value of L determined than other production methods. This is attributed to the native inconsistencies and surface roughness. ICP etch damage of 3 minutes led to a noticeable reduction in the mean value of L from 350 ± 75 nm to 305 ± 43 nm at room temperature. Since the $R_e$ in that case was ~ 870 nm and linearity of EBIC was found with $\alpha$ = -0.5 in both cases, it is likely that the defects reducing diffusion length are not restricted to the sample surface. A likely explanation is that point defects are have been introduced via ICP, another possible explanation is the introduction of surface strain induced by the removal of ~210 nm of material. The damage is created by energetic ion bombardment but in some cases may also consist of changes to near-surface stoichiometry through the preferential loss of one of the lattice elements or deposition of etch residues.

HVPE samples showed a similar value of L = 340 nm and an activation energy of 42 meV was determined by observing the temperature dependence of L. The activation energy matches closely with the ionization energy for Si donors found in previous β-$Ga_2O_3$ studies [64, 80-83]. When these samples were exposed to high energy electron and proton radiation, their diffusion lengths displayed an expected decrease. The continuous CL emission spectrum was unaffected by irradiation, which indicates the introduction of irradiation-induced defects lying outside of the recombination pathways. However, the reduction in the thermal activation energy insists that the defects induced are shallow and their binding is easily thermally overcome. A very interesting effect, which was more pronounced in the proton irradiated study, was a reduction in thermal activation energy and simultaneous increase in asymptotic minority carrier diffusion length, $L_0$. This insists that for high energy particle irradiated samples, the minority carrier diffusion length is higher at higher temperatures. Therefore, we may conclude that irradiation of HVPE grown β-$Ga_2O_3$ tend to introduce defects which counteract the reduction of L by temperature.

## 3.3 Minority Carrier Transport Properties in InAs/GaSb Type II Strain-Layer Superlattice[7]

### 3.3.1 *Prior State of the Art*

Previously, EBIC has been used to determine the minority carrier diffusion length in p-type InAs/GaSb T2SLS structures with much different ML ratios. For example, it has been used to estimate the lifetime of excited carriers in a 8/8 ML ratio InAs/GaSb T2SLS by measuring diffusion length and assuming from Bürkle *et al*. an out-of-plane electron mobility of 1100 $cm^2/Vs$ [93, 94]. Further, EBIC measurements were taken to observe the impact on collection efficiency as influenced by the introduction of an InSb interfacial layer in a 9/17 ML ratio InAs/GaSb structure [8]. Due to the narrow bandgap, any electron beam stimulated emission would be in the IR, and inaccessible to the CL equipment available.

This study applies the method of EBIC to determine the impact of gamma irradiation-induced damage on a 10/10 ML ratio InAs/GaSb T2SLS by observing the minority carrier diffusion length and trap thermal activation energy. Gamma irradiation primarily induces ionization defects, but may also produce some displacement defects. Heavy ions, like protons, more readily generate displacement defects, while gamma more easily creates ionization defects. Studies of

---

[7] Portions of § 3.3 Minority Carrier Transport Properties in InAs/GaSb Type II Strain-Layer Superlattice have been accepted for publication in Journal of Applied Physics, Jonathan Lee, Chris Fredricksen, Elena Flitsiyan, Robert Peale, Leonid Chernyak, Zahra Taghipour, Lilian Casias, Alireza Kazemi, Sanjay Krishna and Stephen Myers. *Impact of temperature and gamma radiation on electron diffusion length and mobility in p-type InAs/GaSb superlattices,* Accepted for publication 31 May 2018.

both types of radiation damage are needed to separate the total ionization dose effects from the displacement effects. Direct measurements of minority carrier diffusion length, *L*, perpendicular to the growth plane (also referred to as “out of plane,” see Figure 28 (b)) by variable temperature EBIC in InAs/GaSb T2SLS, designed as an IR absorber, to study the ionization dose effects from gamma irradiation.

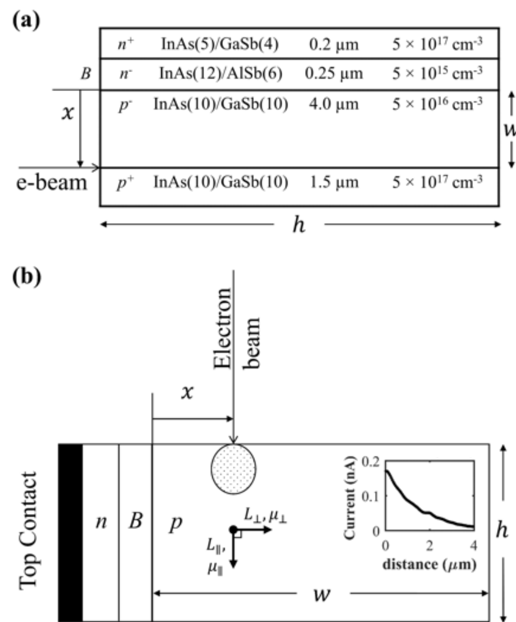


Figure 28. Schematic of the T2SLS structure. (a)The majority carrier type and concentration, periodic ML ratio, and composite layer thicknesses are indicated. The vertical arrow shows the direction for EBIC line-scan, the horizontal arrow indicates the instantaneous electron-beam position. The absorber thickness is denoted by w and the sample lateral dimension by h (not to scale). (b) Illustration of the normal-collector configuration. Top metallic contact, n- and p-type regions, absorber thickness w, and sample lateral dimension h (not to scale), and the electron beam-to-junction distance x, are indicated. Carrier transport anisotropy is indicated by ∥ and ⊥ for L and μ with reference to the growth plane. The inset presents typical sample EBIC data. For both diagrams, the barrier (n-type InAs/AlSb) is indicated by the letter “B”. After ref. [92].

### 3.3.2 *Impact of $^{60}$Co γ-Radiation*

The p-type/barrier/n-type (pBn) structure reported here was grown by Molecular Beam Epitaxy (MBE) on a conductive GaSb substrate [95]. This structure is presented schematically in Figure 28 (a), which indicates carrier concentration and type, number and species of monolayers (ML) in each SL period (e.g. 10/10 for the absorber region) and thicknesses of each region [96]. The bipolar device structure was chosen for analysis due to its potential for practical industrial applications. Specifically, the structure is advantageous due to the higher mobility of minority electrons (relative to holes) in p-type absorber, which dictates faster bipolar IR detector functionality. The inclusion of a barrier layer has been shown to reduce leakage currents from generation-recombination at interfaces [97, 98], further, due to its lower charge density as compared to the absorber layer, the barrier layer accepts most of the local space charge region [99]. The absorption cutoff wavelength can be estimated to be ~ 5.8 µm for a 10/10 ML ratio InAs/GaSb T2SLS [9]. Because of its importance to detector quantum efficiency, we focus on the minority carrier diffusion length within the $5 \times 10^{16}$ $cm^{-3}$-doped 4 µm-thick p-InAs/GaSb absorber (cf. Figure 28 (a)). That the absorber layer is *p*-type allows for longer potential minority carrier diffusion lengths due to the lower effective mass of excited electrons.

Two samples cleaved from the same pBn structure were studied in this work. One was reserved as a control, while the other received a 500 Gy absorbed dose of $^{60}$Co gamma irradiation (Nordion, Inc.) at room temperature in a nitrogen environment. (Determination of the absorbed dose value in Gray = Joules/kg includes the substrate.) Gamma radiation was used in order to simulate exposure to a radiation harsh environment. A Ti (5 nm)/Au (50 nm) Ohmic contact was electron-beam evaporated on the top surface of the structure. The back surface of the samples

(substrate) was contacted with conductive adhesive. Contacts were applied post irradiation to prevent the possibility of secondary radiation.

The EBIC measurements were carried out *in-situ* in a Philips XL-30 SEM. The contacted sample was mounted on an L-shaped aluminum bracket with grounded bottom contact in the normal-collector configuration, Figure 28 (b). The SEM beam accelerating voltage was 30 kV, which gives an electron range $R_e$ ~ 4.8 µm for both InAs and GaSb employing the Kanaya-Okayama approach [28, 100]. The relatively high accelerating voltage can optimize EBIC resolution, accuracy, and signal-to-noise ratio by increasing probe current. Because the EBIC generation region extends laterally by only ~ ½ $R_e$ (cf. Figure 28 (b)), the ratio $R_e/L < 4$ ensures the data are not instrument limited [27]. The sample dimension *h*, which is parallel to the growth plane of the SL (perpendicular to the growth direction, cf. Figure 28), exceeds 5 mm, which is much larger than the electron range ($h \gg R_e$), so that the dimension, *h*, does not limit the collection of generated carriers [22].

The electron beam was scanned along a cleaved edge perpendicular to the growth plane of the layers (cf. Figure 28 (a), (b)) from the top surface to a distance of about 5 µm while recording the induced current. Observing the carrier densities, we may estimate the depletion region width to be approximately 0.4 µm, with ~ 150 nm extending into the InAs/GaSb absorber $p^-$ layer [99]. Carriers diffused from the point of origin at a beam-to-junction distance, *x*, and some move toward the space-charge region at the *n-p* InAs/AlSb - InAs/GaSb junction, which separated the non-equilibrium carriers and swept them for collection. Such cross-sectional line-scans were performed at various locations on the cleaved edge for temperatures ranging from 77 to 273 K.

Minority carriers (holes) generated in the *n*-type region close the *n*-*p* interface (see Figure 28 (a), (b)) do not contribute appreciably to the EBIC signal due to their relatively low mobility ($\mu_p \ll \mu_e$) [101] and the presence of the InAs/AlSb hole-barrier layer blocks hole transport across the junction [102]. The 1.5 µm thick $p^+$ region below the absorber (cf. Figure 28 (a)) should also offer minimal interference due to its overall similarity to the 4 µm-thick 10/10 *p*-InAs/GaSb absorber layer under test.

The minority electron diffusion length, $L_e$, was extracted using methods described in § 2.4

Electron Beam-Induced Current (EBIC) and described in ref. [34]. Equation (7) is the same as used by Hanoka for spherical generation volume and small $v_s$ [103]. Several EBIC line-scans were completed at each temperature and the average value and standard deviation for minority carrier diffusion length were determined.

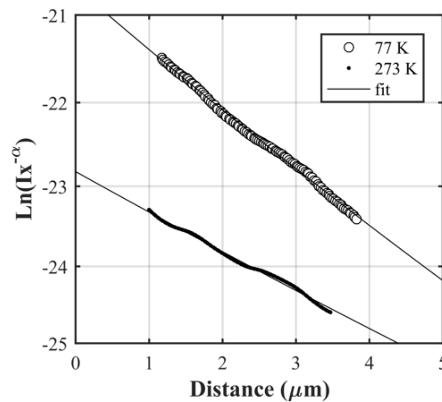


Figure 29. InAs/GaSb T2SLS control-sample EBIC data and linear fit. For temperatures (o) 77 K and (•) 273 K using equation (10) employing linearization coefficient, α = 0. After ref. [92].

The experimental dependence of $\ln(I_E x^{-\alpha})$ on *x* for the control sample is presented for temperatures 77 and 273 K in Figure 29 for $\alpha = 0$. The straight line, found when $\alpha = 0$, implies a small value for $v_s$, below ~1000 cm/s [34]. The diffusion length is determined by the negative

reciprocal of the linear slope. Diffusion length for the control sample was found to increase with temperature, as shown in Figure 30, from the value 1.08 ± 0.20 μm at 77 K to 2.24 ± 0.31 μm at 273 K.

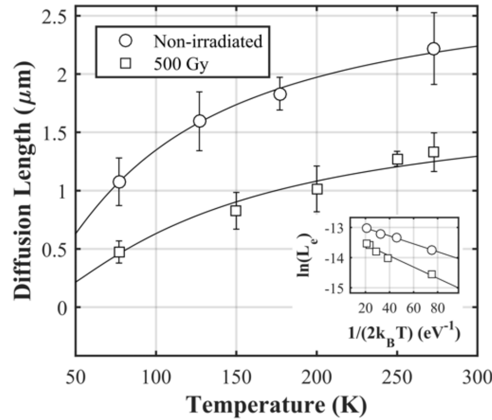


Figure 30. Temperature dependence of electron diffusion length for InAs/GaSb T2SLS. Control sample (circles) and 500 Gy gamma-irradiated sample (squares) with exponential fit (solid line) using equation (11). Inset: Arrhenius plot indicating the corresponding activation energies of 13.1 and 18.6 meV for the non-irradiated and 500 Gy gamma-irradiated samples respectively. After ref. [92].

The minority carrier diffusion length far exceeds the InAs and GaSb single-material layer thicknesses of ~2.5 nm, possibly indicative of low boundary scattering. This behavior is similar to observations in AlGaN/GaN SLs, where the minority carrier diffusion length was also found to exceed the SL layer thicknesses [104]. This compares with other reports for InAs/GaSb T2SLS structures, where shortening of diffusion lengths was attributed to interfacial roughness [93, 105]. Figure 30 further presents EBIC results for the 500 Gy gamma-irradiated sample, where the $L_e$ values are twice smaller than for the control sample, and $E_a$ has increased to 18.6 meV. The decrease in $L_e$ is reasonably attributed to scattering by radiation-induced defects.

The temperature dependence of the minority electron diffusion length is given by equation (11). The value $E_a$ = 13.1 meV was found from the temperature dependence presented as an Arrhenius plot in the Figure 30 inset. This value, which is much smaller than usual bandgaps for mid-wave IR detectors (~ 100 – 400 meV), suggests a thermally activated charge trap or defect level ~ 13.1 meV below the conduction or above valence band. The increase in $E_a$ to ~ 18.6 meV after 500 Gy gamma-irradiation is likely due to the appearance of deeper levels for non-equilibrium carrier recombination, as was previously observed for gamma-irradiated AlGaN/GaN heterostructures [106].

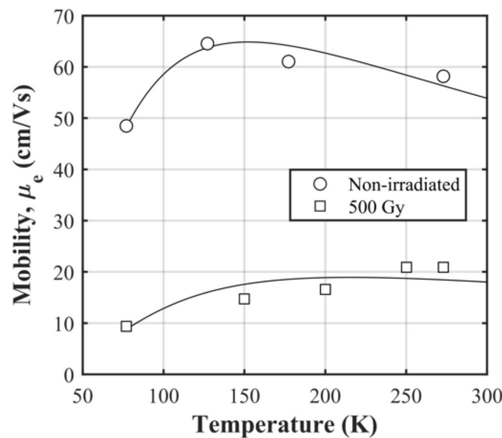


Figure 31. Electron mobility values for InAs/GaSb. Control sample (circles) and 500 Gy gamma irradiated sample (squares) and the corresponding fit (solid lines) using equations (11) and assuming τ = 36 ns [32]. After ref. [92].

The minority carrier lifetime, τ, is estimated from the Einstein relation, equation (11). The lifetime of similar SLS InAs/GaSb structures with ML ratio of 8/8 was determined by TRPL and was found to depend on carrier concentration, therefore at a concentration of $5 \times 10^{16}$ $cm^{-3}$ we assume a temperature independent lifetime of τ ~ 36 ns [107]. The minority electron mobility can thus be estimated by equation (3) and is displayed in Figure 31 along with line of fit. The electron mobility for *n*-type T2SLS with ML ratio of 9/9, measured in the SL growth plane ($\mu_{\parallel}$) by

quantitative mobility spectrum analysis, was found ~ $1 \times 10^4$ $cm^2/Vs$ at 300 K [101]. However, the anisotropy of minority carrier transport leads to a reduction in electron mobility perpendicular to the growth plane – by as much as a factor of 10, according to Bürkle *et al.*, where the electron mobility perpendicular to the growth plane ($\mu_{\perp}$) of a superlattice structure with InAs/(GaIn)Sb of ML ratio 8/8 was measured to be ~ 1100 $cm^2/Vs$, though the overall structure is intrinsically different than this case [93, 94]. Here, the mobility perpendicular to the growth plane for minority electrons in the non-irradiated *p*-type T2SLS with ML ratio 10/10 was found to be ~ 55 $cm^2/Vs$ at 300 K. The comparatively low value of electron mobility is attributed to possible differences in layer content, carrier concentration, ML ratio, and interfacial roughness.

For the non-irradiated sample, there is an apparent shift in the trend of the minority electron mobility near 120 K shown in Figure 31 which is characteristic of this T2SLS structure [96, 101, 108, 109], where a shift in the majority carrier mobility and density was observed for InAs/GaSb SLs with 8/8 and 9/9 periodic ML ratios. In those cases, the inflection was attributed to a shift in the dominant scattering mechanism from impurity scattering at low temperatures to phonon scattering at high temperatures. For the 500 Gy gamma-irradiated sample, the behavior of the mobility suggests a transition of the dominant scattering mechanism may occur at ~ 200 K, and is likely due to scattering on radiation induced defects.

# CHAPTER IV – CONCLUDING REMARKS & DISCUSSION

*"If I have seen further it is by standing on the shoulders of Giants."*

–Isaac Newton

## 4.1 Transport properties in β-$Ga_2O_3$

Majority carrier n-type Si-doped β-$Ga_2O_3$ was investigated for its minority carrier transport properties including minority carrier diffusion length and excited carrier lifetime. According to EBIC measurements carried out on Schottky barrier diodes, the magnitude of L was at or about 350 nm at room temperature and depend on production method, temperature, and, presumably, defect concentration. The surface recombination velocity impact on EBIC measurement was minimal for each case. The diffusion length showed a lower variance in the epitaxially produced samples as compared to the bulk-produced samples, which was attributed to surface quality. Interestingly, the temperature dependence of the diffusion length showed an opposite behavior as compared to GaN. Continuous wave CL measurements demonstrated the primary emission wavelength was approximately 380 nm (3.26 eV) with an 80 nm FWHM and a defect band at 570 nm (2.18 eV). Observed by TRCL, the excited carrier lifetime of the band at 380 nm was around 200 ps, seemingly in conflict with previous investigations using *cathode ray* and light source excitation methods which place minimum $\tau$ ~ 20 ns, however, the lifetime observations generally include a fast and slow component. Furthermore, the sources of excitation in those previous studies are not described quantitatively enough (i.e. length of pulse, temporal resolution) to attempt to estimate the reasons for these lifetime variances. The as-

grown trap state thermal activation energy was found to be around 40 meV and was attributed to H inclusions or native $V_O$ defects.

### 4.1.1 Radiation Impact

The impact of 1.5 MeV electron, and 10 MeV proton irradiation was observed and quantified by measurement of L and τ. In addition, electron (proton) irradiation was found to reduce majority carrier electron concentration at a removal rate of 4.9 $cm^{-1}$ (235 $cm^{-1}$). This translated to an impact factor of 50 times for proton to electron impact. The room temperature values of L and τ decreased monotonically in response to electron and proton irradiation, as well as the thermal activation energy. In contrast, the asymptotic minority carrier diffusion length increased monotonically for each radiation applied. The unaltered CL spectra before and after irradiation suggests that the trap-assisted recombination pathway remains unchanged. For electron irradiation, the reduction in lifetime suggests that this pathway became more easily taken. This is confirmed by the simultaneous decrease in thermal activation energy, which indicates traps are more easily evacuated by thermal influence. For proton irradiation, there was an increase in excited carrier lifetime. The threshold temperature for diffusion length prominence of irradiated samples was about 58 °C. The carrier removal rates reveal a radiation hardness that is on par with GaN [72], and irradiation damage can be curtailed by annealing at temperatures of about 400 °C [69]. The behavior of the diffusion length with temperature after radiation damage indicates a material which is suitable for space borne applications.

## 4.2 Transport Properties of InAs/GaSb Type-II Strain-Layer Superlattice

The minority electron transport properties were probed by EBIC as a function of temperature. The diffusion length increased with temperature with an activation energy of 13.1 meV. Electron mobilities were estimated based on the experimentally obtained L values perpendicular to the growth plane and independent lifetime studies.

### *4.2.1 Radiation Impact*

Gamma irradiation with a modest 500 Gy dose decreased electron diffusion length by twice and correspondingly increased the thermal activation energy to 18.6 meV. The room temperature control sample minority electron mobility was found to be ~ 55 $cm^2$/Vs and reduced to ~ 21 $cm^2$/Vs after 500 Gy gamma irradiation. The increase in activation energy and decrease in mobility is attributed to radiation-induced scattering centers and deep levels for non-equilibrium carrier recombination.

# APPENDIX A – PUBLISHED WORKS

**Lee, Jonathan**, Chris Fredricksen, Elena Flitsiyan, Robert Peale, Leonid Chernyak, Zahra Taghipour, Lilian Casias, Alireza Kazemi, Sanjay Krishna, and Stephen Myers, *Impact of temperature and gamma radiation on electron diffusion length and mobility in p-type InAs/GaSb superlattices*. Journal of Applied Physics*, 2018*. **Accepted for publication**.

**Lee, Jonathan**, Elena Flitsiyan, Leonid Chernyak, Jiancheng Yang, Fan Ren, Stephen J. Pearton, Boris Meyler and Y. Joseph Salzman, *Effect of 1.5 MeV Electron Irradiation on β-$Ga_2O_3$ Carrier Lifetime and Diffusion Length.* Applied Physics Letters*, 2018.* ***112****(082104): p. 1-11.*

Yang, Jiancheng, Zhiting Chen, Fan Ren, Stephen J. Pearton, Gwangseok Yang, Jihyun Kim, **Jonathan Lee**, Elena Flitsiyan, Leonid Chernyak and Akito Kuramata, *10 MeV proton damage in β−$Ga_2O_3$ Schottky rectifiers.* Journal of Vacuum Science and Technology B, *2018.* ***36****(011206): p. 1-4.*

Yang, Jiancheng, Fan Ren, Rohit Khanna, Kristen Bevlin, Dwarakanath Geerpuram, Li-Chun Tung, Jingyu Lin, Hongxing Jiang, **Jonathan Lee**, Elena Flitsiyan, Leonid Chernyak, S. J. Pearton, and Akito Kuramata, *Annealing of dry etch damage in metallized and bare (-201) $Ga_2O_3$.* Journal of Vacuum Science and Technology B*, 2017.* ***35****(5): p. 1-5.*

**Lee, Jonathan,** Elena Flitsiyan, Leonid Chernyak, Joseph Salzman and Boris Meyler, *Effects of Gamma Irradiation on AlGaN-Based High Electron Mobility Transistors.* Electrochemical Society Journal of Solid State Science and Technology, *2017.* ***6****(11): p. S3063-S3066.*

**Lee, Jonathan**, Elena Flitsiyan, Leonid Chernyak, Shihyun Ahn, Fan Ren, Lin Yuna, Stephen J. Pearton, Jihyun Kim, Boris Meyler, and Joseph Salzman, *Optical Signature of the Electron Injection in $Ga_2O_3$.* Electrochemical Society Journal of Solid State Science and Technology, *2017.* ***6****(2). p. Q3049-Q3051.*

**Lee, Jonathan**, Anupama Yadav, Michael Antia, Valentina Zaffino, Elena Flitsiyan, Leonid Chernyak, Joseph Salzman, Boris Meyler, Shihyun Ahn, Fan Ren, and Stephen J. Pearton, *Low Dose $^{60}$Co Gamma-Irradiation Effects on Electronic Carrier Transport and DC Characteristics of*

*AlGaN/GaN High-Electron-Mobility Transistors.* Radiation Effects and Defects in Solids, *2016.* ***172****(3-4). p. 250-256.*

# APPENDIX B – RELATED ONGOING WORK

B.1 Temperature Influence on Continuous Wave CL Intensity

The intensity of continuous wave CL emission is being reviewed in accordance with equation (12), namely:

$$I_{CL}(T) = \frac{A}{\left(1 + Bexp\left(-\frac{E_a}{k_B T}\right)\right)} \quad (12)$$

This Fermi-Dirac statistical description should reveal the thermal activation energy related to CL emission intensity thermal quenching. Evidence for this behavior includes two spectra collected the HVPE reference sample (from the study in § 3.2.5 Impact of 1.5 MeV Electron Irradiation) reveal an intensity reduction on increasing temperature from 80 K to 295 K.

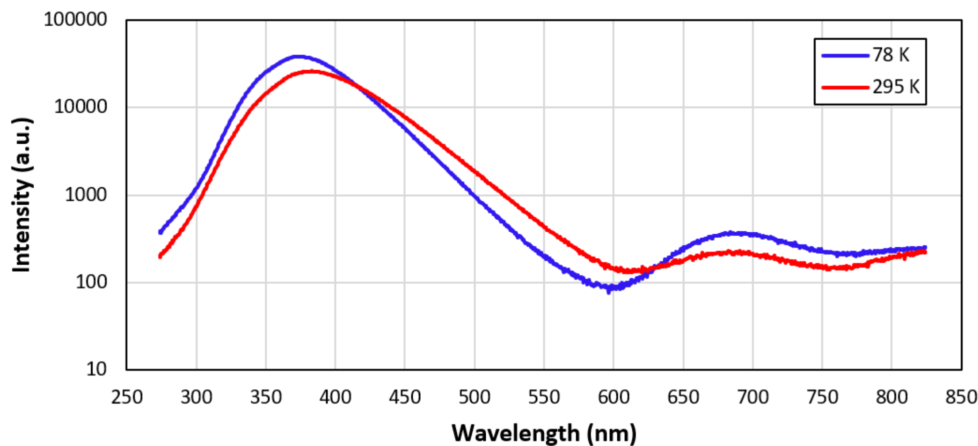


Figure 32. Continuous wave CL spectra temperature comparison for HVPE produced β-$Ga_2O_3$. The spectra are shown for 78 K (blue) and 295 K (red) collected at 10 kV using the Attolight instrument.

Also, the maximum wavelength (in Figure 32) experienced a red shift from 375 nm at 80 K to 383 nm for 295 K. Crystals grown from 4N grade powder using the Verneuil method and showed an adherence to equation (12) with an activation energy of 50 meV for the band centered at 2.64 eV (470 nm) using PL [64]. The influence of temperature is apparent and should be characterized.

B.2 Electromigration of Ni/Au in β-$Ga_2O_3$

The application of high reverse-bias voltage to Schottky rectifiers resulted in device inoperability (electrically open circuit). Reverse-bias voltages of 0, -50 and -70 V were applied to 105 μm diameter circular Ni/Au films were imaged using the Philips XL-30 SEM at 30 kV. Upon the application of -70 V bias, the junction electrically failed and was re-imaged. The results are displayed in Figure 33.

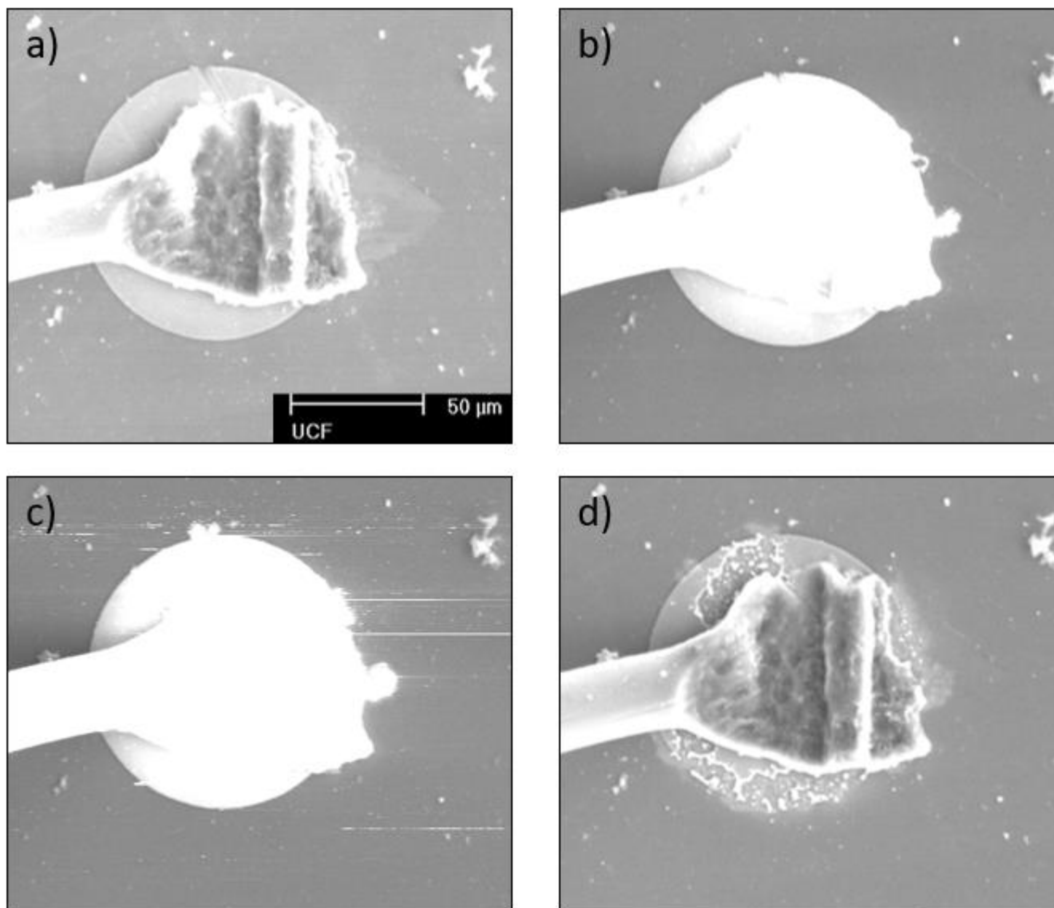


Figure 33. Presumed electromigration in β-$Ga_2O_3$ as shown by SEM. Images collected at 30 kV using the Philips XL-30 for (a) before, (b) during -20 V, (c) -50 V, and (d) after applying dc reverse-bias of -70 V.

Evidence of electromigration appeared at -50 V reverse-bias, and can be seen in Figure 33 (c). It is apparent when comparing the top of the Schottky contact in Figure 33 (a) and (c) that the electromigration persists along the regions which were noticeably damaged before reverse-bias application. This occurs because the crystal is mechanically damaged and therefore weaker against the introduction of metal atoms. The most dramatic observation occurred at -70 V reverse-bias, when the diode failed. Large sections of the diode surface were missing, shown in Figure 33 (d), and the change in contrast suggests an alteration in the local electronic property to become more metallic.

The open circuit measurement has two generally likely origins: (1) that adding metal ions (barrier materials: Ni 20 nm and Au 80 nm) to β-$Ga_2O_3$ induces insulative behavior, or (2) the aluminum metal wires used for contact bonding alloyed with the gold top part of the Schottky contact which is a microcircuit failure known as *white* ($Au_5Al_2$) or *purple plague* ($AuAl_2$) nicknamed for their apparent color. The first possibility can nearly be discounted by observing Figure 33 (c), during the -50 V reverse-bias, notice the brightness of the contact wire. The brightness in SEM image indicates a higher electron count stimulated by the electron beam, therefore conclude the contact is brighter because the 'electrical pressure' is higher for electrons which are electrically connected. Since the presumably electromigrated areas are brightened in that image, they are electrically connected – at least after some degree of the effect. The second possibility is much more likely due to the elemental purity of the materials chosen and the ease at which Au-Al alloys are formed.

## B.3 Impact of Alpha Irradiation on $\beta$-$Ga_2O_3$

Studies into the impact of high energy radiations continue with 18 MeV alpha particles. The I-V characteristics are presented including the ideality factor and current coefficient from

$$J(T) = J_0 \exp\left(\frac{qV}{\eta k_B T}\right) \tag{19}$$

where η is the ideality factor, q is the fundamental charge and V is the applied voltage. These factors are presented with their respective sample data for the reference sample, Figure 34, and the 5 × $10^{14}$ $cm^{-2}$ 18 MeV alpha irradiated sample, Figure 35.

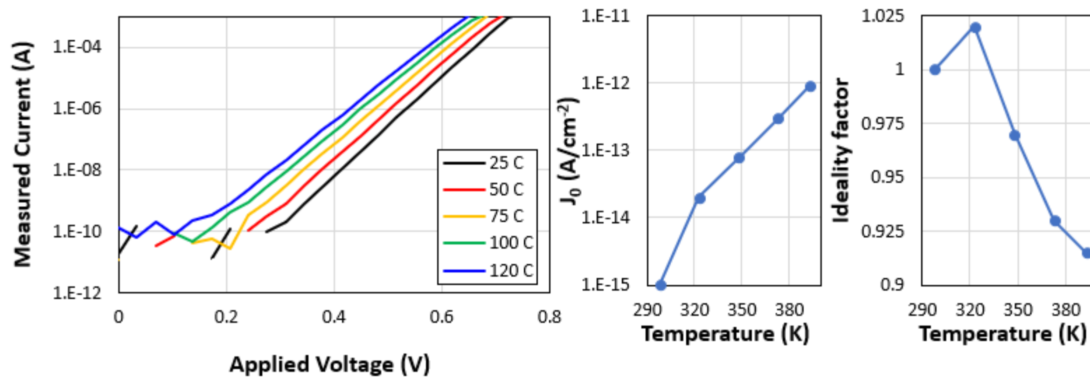


Figure 34. I-V characteristics of $\beta$-$Ga_2O_3$ reference sample as a function of temperature.

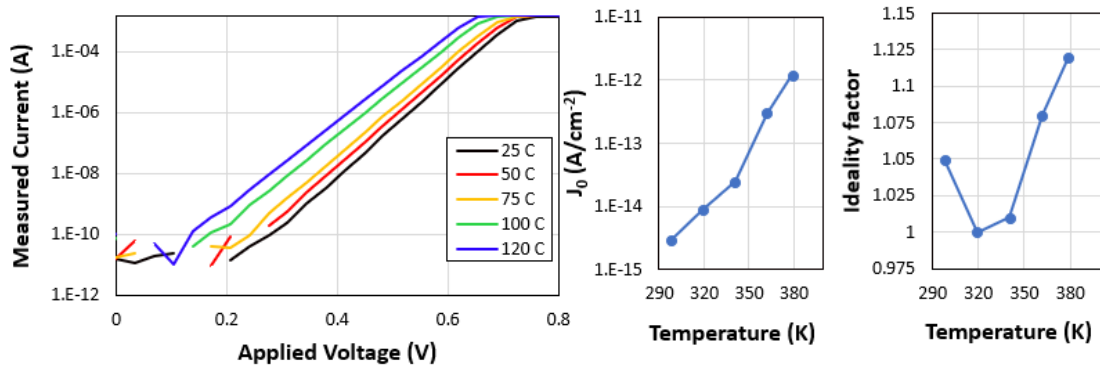


Figure 35. I-V characteristics of $\beta$-$Ga_2O_3$ alpha particle irradiated sample as a function of temperature.

# APPENDIX C – OPTICAL CONSIDERATIONS

One must take into account grating efficiency to ensure appropriate interpretation of results. Dispersion was accomplished by blazed gratings, whose efficiencies are not unity across the spectrum demanded by the user. There were two gratings used throughout these studies.

Table 5. Dispersion grating parameters by instrument.

| Instrument | Line density ($mm^{-1}$) | Blazed at (nm) | Blaze angle (°) |
|---|---|---|---|
| Philips XL-30 | 1200 | 500 | 31.0 |
| Attolight | 150 | 500 | 4.29 |

Grating dispersion can have a variance in unity by polarization due to the nature of diffraction. For blaze angles less than 5° polarization effects are essentially not present, but strong anomalies can be found for gratings between 22° and 38°. The efficiency of both gratings is estimated to be 50 % at 300 nm. Due to the low efficiencies of the gratings near 250 nm, an alternate grating was used (600 lines/mm blazed at 300 nm) to rule out band-to-band recombination in β-$Ga_2O_3$ studies.

REFERENCES


1. L. Chernyak, G. Nootz, and A. Osinsky, *Electron. Lett.* **37**, 922 14 (2001).
2. S. I. Stepanov, V. I. Nikolaev, V. E. Bougrov, and A. E. Romanov, *Rev. Adv. Mater. Sci.* **44**, 63 (2016).
3. E. Chikoidze, A. Fellous, A. Perez-Tomas, G. Sauthier, T. Tchelidze, C. Ton-That, T. T. Huynh, M. Phillips, S. Russell, M. Jennings, B. Berini, F. Jomard, and Y. Dumont, *Materials Today Physics* **In Press**, doi: 10.1016/j.mtphys.2017.10.002 (2017).
4. S. W. S. McKeever. Cambridge Solid State Science Series. Cambridge: Press Syndicate of University of Cambridge. 376. (1985).
5. G. J. Hurford, R. A. Schwartz, S. Krucker, R. P. Lin, D. M. Smith, and N. Vilmer, *The Astrophysical Journal Letters* **595**, L77 (2003).
6. A. Ionascut-Nedelcescu, C. Carlone, A. Houdayer, H. J. von Bardeleben, J.-L. Cantin, and S. Raymond, *IEEE Trans. Nucl. Sci.* **49**, 2733 (2002).
7. Y.-K. Kuo, and W.-W. Lin, *Jpn. J. Appl. Phys., Part 1* **41**, 73 1 (2002).
8. D. Zuo, P. Qiao, D. Wasserman, and S. L. Chuang, *Appl. Phys. Lett.* **102**, 141107 (2013).
9. P. Christol, and J. B. Rodriguez. in *SPIE Internation Conference on Space Optics*. Tenerife, Canary Islands, Spain. (2014).
10. M. Eckstein, and H.-U. Habermeier, *J. Phys. IV* **1**, 23 (1991).
11. S. Boggs, and D. Krinsley. New York: Cambridge University Press. (2009).
12. L. Chernyak, A. Osinsky, and A. Schulte, *Solid-State Electron.* **45**, 1687 9 (2001).
13. O. Lopatiuk-Tirpak, L. Chernyak, L. J. Mandalapu, Z. Yang, J. L. Liu, K. Gartsman, Y. Feldman, and Z. Dashevsky, *Appl. Phys. Lett.* **89**, 142114 (2006).
14. O. Lopatiuk-Tirpak, L. Chernyak, Y. L. Wang, F. Ren, S. J. Pearton, K. Gartsman, and Y. Feldman, *Appl. Phys. Lett.* **90**, 172111 (2007).
15. H. Lu, X. A. Cao, S. F. LeBoeuf, H. C. Hong, E. B. Kaminsky, and S. D. Arthur, *J. Cryst. Growth* **291**, 82 (2006).
16. S. J. Rosner, G. Girolami, H. Marchand, P. T. Fini, J. P. Ibbetson, L. Zhao, S. Keller, U. K. Mishra, S. P. DenBaars, and J. S. Speck, *Appl. Phys. Lett.* **74**, 2035 (1999).
17. E. J. R. Vesseur, T. Coenen, H. Caglayan, N. Engheta, and A. Polman, *Phys. Rev. Lett.* **110**, 1-4 (2013).
18. C. E. Hofmann, E. J. R. Vesseur, L. A. Sweatlock, H. J. Lezec, F. J. G. d. Abajo, A. Polman, and H. A. Atwater, *Nano Lett.* **7**, 3612 (2007).
19. M. Yoshikawa, K. Matsuda, Y. Yamaguchi, T. Matsunobe, Y. Nagasawa, H. Fujino, and T. Yamane, *J. Appl. Phys.* **92**, 7153 (2002).
20. C. Donolato, *Phys. Status Solidi A* **141**, K131 (1994).
21. D. E. Ioannou, and C. A. Dimitriadis, *IEEE Trans. Electron Devices* **ED-29**, 445 3 (1982).
22. O. Kurniawan, and V. K. S. Ong in *Optoelectronic and Microelectronic Materials and Devices*. Perth, WA, Australia: IEEE. (2006).
23. H. J. Leamy, *J. Appl. Phys.* **53**, 51 6 (1982).
24. P. Corfdir, P. Lefebvre, L. Balet, S. Sonderegger, A. Dussaigne, T. Zhu, D. Martin, J.-D. Ganière, N. Grandjean, and B. Deveaud-Plédran, *J. Appl. Phys.* **107**, 043524 (2010).

25. X. Fu, G. Jacopin, M. Shahmohammadi, R. Liu, M. Benameur, J.-D. Ganiere, J. Feng, W. Guo, Z.-M. Liao, B. Deveaud, and D. Yu, *ACS Nano* **8**, 3412 (2014).
26. M. A. Xapsos, G. P. Summers, C. C. Blatchley, C. W. Colerico, E. A. Burke, S. R. Messenger, and P. Shapiro, *IEEE Trans. Nucl. Sci.* **41**, 6 (1994).
27. K. L. Luke, O. von Roos, and L.-J. Cheng, *J. Appl. Phys.* **57**, 1978 6 (1985).
28. O. Kurniawan, and V. K. S. Ong, *Scanning* **29**, 280 6 (2007).
29. F. Berz, and H. K. Kuiken, *Solid-State Electron.* **19**, 437 6 (1976).
30. L. Jastrzebski, J. Lagowski, and H. C. Gatos, *Appl. Phys. Lett.* **27**, 537 (1975).
31. E. B. Yakimov, A. Y. Polyakov, N. B. Smirnov, I. V. Shchemerov, J. Yang, F. Ren, G. Yang, J. Kim, and S. J. Pearton, *J. Appl. Phys.* **123**, 18 (2018).
32. J.-M. Bonard, and Jean-Daniel Ganiere, *J. Appl. Phys.* **79**, 6987 9 (1996).
33. C. J. Wu, and D. B. Wittry, *J. Appl. Phys.* **49**, 5 (1977).
34. C. C. Tan, V. K. S. Ong, and K. Radhakrishnan, *IEEE Trans. Electron Devices* **60**, 3541 10 (2013).
35. W. C. Burdett, O. Lopatiuk, A. Osinsky, S. J. Pearton, and L. Chernyak, *Superlattice Microst.* **34**, 55 (2004).
36. O. Lopatiuk-Tirpak, L. Chernyak, F. X. Xiu, J. L. Liu, S. Jang, F. Ren, S. J. Pearton, K. Gartsman, Y. Feldman, A. Osinsky, and P. Chow, *J. Appl. Phys.* **100**, 086101 (2006).
37. J. Lee, E. Flitsiyan, L. Chernyak, J. Salzman, and B. Meyler, *ECS J. Solid State Sci. Technol.* **6**, S3063 11 (2017).
38. S. Ahn, C. Dong, W. Zhu, B.-J. Kim, Y.-H. Hwang, F. Ren, S. J. Pearton, G. Yang, J. Kim, E. Patrick, B. Tracy, D. J. Smith, and I. I. Kravchenko, *J. Vac. Sci. Technol. B* **33**, 051208 (2015).
39. L. Liu, Y.-H. Hwang, Y. Xi, F. Ren, V. Caciun, S. J. Pearton, G. Yang, H.-Y. Kim, and J. Kim, *J. Vac. Sci. Technol. B* **32**, 2 (2014).
40. S. J. Pearton, Ya-Shi Hwang, and F. Ren, *JOM* **67**, 1601 7 (2015).
41. B. Luo, Jihyun Kim, F. Ren, A. G. Baca, R. D. Briggs, B. P. Gila, A. H. Onstine, K. K. Allums, C. R. Abernathy, S. J. Pearton, R. Dwivedi, T. N. Fogarty, and R. Wilkins, *Electrochem. Solid-State Lett.* **6**, G31 3 (2003).
42. A. Y. Polyakov, N. B. Smirnov, A. V. Govorkov, and A. V. Markov, *J. Appl. Phys.* **98**, 033529 (2005).
43. S. A. Vitusevich, N. Klein, A. E. Belyaev, S. V. Danylyuk, M. V. Petrychuk, R. V. Konokova, A. M. Kurakin, A. E. Rengevich, A. Yu. Avksentyev, B. A. Danilchenko, V. Tilak, J. Smart, A. Vertiatchikh, and L. F. Eastman, *Phys. Status Solidi A* **195**, 101 1 (2003).
44. B. Luo, J. W. Johnson, F. Ren, K. K. Allums, C. R. Abernathy, S. J. Pearton, A. M. Dabiran, A. M. Wowchack, C. J. Polley, P. P. Chow, D. Schoenfeld, and A. G. Baca, *Appl. Phys. Lett.* **80**, 604 4 (2002).
45. O. Aktas, A. Kuliev, V. Kumar, R. Schwindt, S. Toshkov, D. Costescu, J. Stubbins, and I. Adesida, *Solid-State Electron.* **48**, 471 (2004).
46. D. W. Jenkins, John D. Dow, and Min-Hsiung Tsai, *J. Appl. Phys.* **72**, 4130 9 (1992).
47. L. E. Ramos, J. Furthmuller, F. Bechstedt, L. M. R. Scolfaro, and J. R. Leite, *J. Phys.: Condens. Matter* **14**, 2577 10 (2002).
48. J. L. Lyons, and Chris G. Van de Walle, *NPJ Computational Materials* **3**, (2017).
49. P. Boguslawski, E. L. Briggs, and J. Bernholc, *Phys. Rev. B* **51**, 17255 23 (1995).

50. G. A. Umana-Membreno, J. M. Dell, T. P. Hessler, B. D. Nener, G. Parish, L. Faraone, and U. K. Mishra, *Appl. Phys. Lett.* **80**, 4354 23 (2002).
51. D. C. Look, D. C. Reynolds, J. W. Hemsky, J. R. Sizelove, R. L. Jones, and R. J. Molnar, *Phys. Rev. Lett.* **79**, 2273 12 (1997).
52. H. Y. Xiao, Fei Gao, X. T. Zu, and W. J. Weber, *J. Appl. Phys.* **105**, 123527 (2009).
53. V. V. Emtsev, V. Yu. Davydov, V. V. Kozlovskii, V. V. Lundin, D. S. Poloskin, A. N. Smirnov, N. M. Shmidt, A. S. Usikov, J. Aderhold, H. Klausing, D. Mistele, T. Rotter, J. Stemmer, O. Semchinova, and J. Graul, *Semicond. Sci. Technol.* **15**, 73 1 (2000).
54. S. Sonderegger. École polytechnique fédérale de Lausanne. Start Page (2007).
55. J. Lee, A. Yadav, M. Antia, V. Zaffino, E. Flitsiyan, L. Chernyak, J. Salzman, B. Meyler, S. Ahn, F. Ren, and S. J. Pearton, *Radiat Eff. Defects Solids* **172**, 250 (2017).
56. S. J. Pearton, R. Deist, F. Ren, L. Liu, A. Y. Polyakov, and J. Kim, *J. Vac. Sci. Technol. A* **31**, 050801 (2013).
57. A. L. Bogorad, J. J. Likar, S. K. Moyer, A. J. Ditzler, G. P. Doorley, and R. Herschitz in *Radiation Effects Data Workshop*. IEEE. 124-130 (2008).
58. T. Harwig, F. Kellendonk, *J. Solid State Chem.* **24**, 255 (1978).
59. G. Blasse, and A. Bril, *J. Phys. Chem. Solids* **31**, 707 (1970).
60. K. Shimamura, E. G. Villora, T. Ujiie, and K. Aoki, *Appl. Phys. Lett.* **92**, 201914 (2008).
61. J. B. Varley, J. R. Weber, A. Janotti, and C. G. V. d. Walle, *Appl. Phys. Lett.* **97**, 142106 (2010).
62. J. B. Varley, A. Janotti, C. Franchini, and C. G. Van de Walle, *Phys. Rev. B* **85**, 8 (2012).
63. E. G. Víllora, K. Hatanaka, H. Odaka, T. Sugawara, T. Miura, H. Fukumura, and T. Fukuda, *Solid State Communications* **127**, 385 (2003).
64. L. Binet, and D. Gourier, *J. Phys. Chem. Solid* **59**, 1241 (1998).
65. V. I. Vasil'tsiv, Ya M. Zakharko, and Ya I. Rym, *UKRAINSKII FIZICHESKII ZHURNAL* **33**, 1320 9 (1988).
66. S. Ahn, Y. Lin, F. Ren, S. Oh, Y. Jung, G. Yang, J. Kim, M. A. Mastro, J. K. Hite, C. R. Eddy Jr., S. J. Pearton, *J. Vac. Sci. Technol. B* **34**, 041213 (2016).
67. J. Yang, F. Ren, S. J. Pearton, G. Yang, J. Kim, and A. Kuramata, *J. Vac. Sci. Technol. B* **35**, 3 (2017).
68. J. Lee, E. Flitsiyan, L. Chernyak, J. Yang, F. Ren, S. J. Pearton, B. Meyler, and Y. J. Salzman, *Appl. Phys. Lett.* **112**, 082104 (2018).
69. J. Yang, F. Ren, R. Khanna, K. Bevlin, D. Geerpuram, L.-C. Tung, J. Lin, H. Jiang, J. Lee, E. Flitsiyan, L. Chernyak, S. J. Pearton, and A. Kuramata, *J. Vac. Sci. Technol. B* **35**, 5 (2017).
70. S. Ohira, and N. Arai, *Physica Status Solidi C* **5**, 3116 (2008).
71. J. Yang, S. Ahn, F. Ren, S. J. Pearton, R. Khanna, K. Bevlin, D. Geerpuram, and A. Kuramata, *J. Vac. Sci. Technol. B* **35**, 031205 (2017).
72. J. Yang, Z. Chen, F. Ren, S. J. Pearton, G. Yang, J. Kim, J. Lee, E. Flitsiyan, L. Chernyak, and A. Kuramata, *J. Vac. Sci. Technol. B* **36**, 011206 (2018).
73. S. Ahn, Y.-H. Lin, and F. Ren, *J. Vac. Sci. Technol. B* **34**, 041213 (2016).
74. J. Yang, F. Ren, S. J. Pearton, G. Yang, J. Kim, and A. Kuramata, *J. Vac. Sci. Technol. B* **35**, 031208 (2017).

75. G. Yang, S. Jang, F. Ren, S. J. Pearton, and J. Kim, *ACS Applied Material Interfaces* **9**, 46 (2017).
76. P. Weiser, M. Stavola, W. B. Fowler, Y. Qin, and S. Pearton, *Appl. Phys. Lett.* **112**, 232104 (2018).
77. P. D. C. King, I. McKenzie, and T. D. Veal, *Appl. Phys. Lett.* **96**, 062110 (2010).
78. T. Oshima, T. Okuno, N. Arai, N. Suzuki, S. Ohira, and S. Fujita, *Appl. Phys. Express* **1**, 11202 1 (2008).
79. D. S. H. Chan, V. K. S. Ong, and J. C. H. Phang, *IEEE Trans. Electron Devices* **42**, 963 5 (1995).
80. T. Oishi, Y. Koga, K. Harada, and M. Kasu, *Appl. Phys. Express* **8**, 031101 (2015).
81. K. Irmscher, Z. Galazka, M. Pietsch, R. Uecker, and R. Fornari, *J. Appl. Phys.* **110**, 063720 (2011).
82. J. Lee, E. Flitsiyan, L. Chernyak, S. Ahn, F. Ren, L. Yuna, S. J. Pearton, J. Kim, B. Meyler, and J. Salzman, *ECS J. Solid State Sci. Technol.* **6**, Q3049 (2017).
83. N. T. Son, K. Goto, K. Nomura, Q. T. Thieu, R. Togashi, H. Murakami, Y. Kumagai, A. Kuramata, M. Higashiwaki, A. Koukitu, S. Yamakoshi, B. Monemar, and E. Janz, *J. Appl. Phys.* **120**, 235703 (2016).
84. L. N. Cojocaru, *Radiation Effects* **21**, 157 (1974).
85. A. Yadav, C. Schwarz, M. Shatkhin, L. Wang, E. Flitsiyan, L. Chernyak, L. Lu, Y. H. Hwang, F. Ren, S. J. Pearton, and I. Lubomirsky, *ECS Transactions* **61**, 171 4 (2014).
86. L. Chernyak, W. Burdett, M. Klimov, and A. Osinsky, *Appl. Phys. Lett.* **82**, 3680 21 (2003).
87. M. Yamaguchi, T. Takamoto, K. Araki, M. Imaizumi, N. Kojima, and Y. Ohshita in *2011 Conference on Lasers and Electro-Optics (CLEO)*. Baltimore, MD, USA: IEEE. (2011).
88. S. Oh, Y. Jung, M. A. Mastro, J. K. Hite, C. R. Eddy Jr., and J. Kim, *Opt. Express* **23**, 28300 22 (2015).
89. B. Theys, V. Sallet, F. Jomard, A. Lusson, J. Rommeluere, and Z. Teukam, *J. Appl. Phys.* **91**, 3922 6 (2002).
90. W. Mi, Caina Luan, Zhao Li, Cansong Zhao, Xianjin Feng, and Jin Ma, *Opt. Mater.* **35**, 2624 (2013).
91. P. D. C. King, and T. D. Veal, *J. Phys.: Condens. Matter* **23**, 334214 (2011).
92. J. Lee, C. Fredricksen, E. Flitsiyan, R. Peale, L. Chernyak, Z. Taghipour, L. Casias, A. Kazemi, S. Krishna, and S. Myers, *J. Appl. Phys.* (2018).
93. J. V. Li, S. L. Chang, E. M. Jackson, and E. Aifer, *Appl. Phys. Lett.* **85**, 1984 11 (2004).
94. L. Bürkle, F. Fuchs, R. Kiefer, W. Pletschen, R. Sah, and J. Schmitz. in *Materials Research Society Symposium Proceedings*. Materials Reseach Society. (1999).
95. E. Plis, S. Annamalai, K. T. Posani, S. Krishna, R. A. Rupani, and S. Ghosh, *J. Appl. Phys.* **100**, 014510 (2006).
96. T. V. C. Rao, J. Antoszewski, L. Faraone, J. B. Rodriguez, E. Plis, and S. Krishna, *Appl. Phys. Lett.* **92**, 012121 (2008).
97. J. R. Pedrazzani, S. Maimon, and G. W. Wicks, *Electron. Lett.* **44**, 1487 25 (2008).
98. E. A. Plis, *Adv. Electron.* **2014**, (2014).
99. S. M. Sze. New York: Wiley. (1985).
100. K. Kanaya, S. Okayama, *J. Phys. D: Appl. Phys.* **5**, 43 (1972).

101. T. V. C. Rao, J. Antoszewski, J. B. Rodriguez, E. Plis, S. Krishna, and L. Faraone, *J. Vac. Sci. Technol. B* **26**, 1081 3 (2008).
102. D. A. Ramirez, E. A. Plis, S. Myers, L. A. Treider, E. Garduno, C. P. Morath, V. M. Cowan, and S. Krishna. in *Nanophotonics and Macrophotonics for Space Environments VIII*. San Diego, California, United States: SPIE Proceedings. (2014).
103. J. I. Hanoka, R. O. Bell, *Annu. Rev. Mater. Sci.* **11**, 353 (1981).
104. L. Chernyak, A. Osinsky, V. N. Fuflyigin, J. W. Graff, and E. F. Schubert, *IEEE Trans. Electron Devices* **48**, 433 3 (2001).
105. C. A. Hoffman, J. R. Meyer, E. R. Youngdale, F. J. Bartoli, R. H. Miles, and L. R. Ram-Mohan, *Solid-State Electron.* **37**, 1203 4-6 (1994).
106. C. Schwarz, A. Yadav, M. Shatkhin, E. Flitsiyan, L. Chernyak, V. Kasiyan, L. Liu, Y. Y. Xi, F. Ren, S. J. Pearton, C. F. Lo, J. W. Johnson, and E. Danilova, *Appl. Phys. Lett.* **102**, 062102 (2013).
107. B. Klein, N. Gautam, E. Plis, T. Schuler-Sandy, T. J. Rotter, and S. Krishna, *J. Vac. Sci. Technol. B* **32**, 2 (2014).
108. C. Cervera, J. B. Rodriguez, J. P. Perez, H. Ait-Kaci, R. Chaghi, L. Konczewicz, S. Contreras, and P. Christol, *J. Appl. Phys.* **106**, 033709 033709 (2009).
109. A. Haddadi, R. Chevallier, A. Dehzangi, and M. Razeghi, *Appl. Phys. Lett.* **110**, 101104 (2017).